Master Dissertation

Inatel
Instituto Nacional de Telecomunicações

# On the Metasurface Integration and Design for Wave Manipulation Improvement of Antenna Systems

BRUNO FERREIRA GOMES

JULY / 2024




# ON THE METASURFACE INTEGRATION AND DESIGN FOR WAVE MANIPULATION IMPROVEMENT OF ANTENNA SYSTEMS

BRUNO FERREIRA GOMES

Dissertation presented to the National Institute of Telecommunications(INATEL) - Brazil for obtaining the title of Master in Telecommunications.

SUPERVISOR: Prof. Dr. Jorge Ricardo Mejía Salazar.

Santa Rita do Sapucaí
2024

Gomes, Bruno Ferreira
G633o
On the Metasurface Integration and Design for Wave Manipulation Improvement of Antenna Systems Bruno Ferreira Gomes– Santa Rita do Sapucaí, 2024.
65p.

Orientador: Prof. Dr. Jorge Ricardo Mejia Salazar
Dissertação de Mestrado em Telecomunicações – Instituto Nacional de Telecomunicações – INATEL.
Inclui bibliografia.

1. Metamateriais 2. Metasuperfícies 3. Metantenas 4. Arranjo de Antenas. 5 Diagrama de Radiação. I. Salazar, Jorge Ricardo Mejia II. Instituto Nacional de Telecomunicações – INATEL. III. Título.

CDU 621.39

Biblioteca "Ministro Olavo Bilac Pinto"

Ficha Catalográfica elaborada pelo Bibliotecário da Instituição
CRB6-2718 – Paulo Eduardo de Almeida

**APPROVAL PAGE**

Thesis presented and approved on 00 / 00 / 2024, by the judging committee:

---

Prof. Dr. Jorge Ricardo Mejía-Salazar
INATEL

---

Prof. Dr. Arismar Cerqueira Sodre Junior
INATEL

---

Prof. Dr. Daniel Chagas do Nascimento
ITA

---

**Graduate Head, Master program**
**(INATEL)**
Prof. Dr. José Marcos Camara Brito

*”Si vis pacem, para bellum”*

*Unknown*

*A dedication to my beloved mother, who was always by my side and was my dearest supporter.*

# Acknowledgments

First and foremost, I wish to express my gratitude to God for always guiding my path, supporting me through periods of sadness as well as moments of happiness, and allowing me to experience both in various ways so that I could grow and become a better person. I am also thankful for all the opportunities He has provided me in life, which have brought me to where I am today.

I dedicate this paragraph to expressing my profound gratitude to my beloved parents, who have always stood by my side in my decisions, supporting me in every possible way to help make this a reality. To my father, Alexandre, my role model in life, I am deeply grateful for your constant presence, love, care, guidance, and for being the best teacher I could ever ask for. From as early as I can remember, you have been my hero and true inspiration. My aspiration has always been to emulate you, a man of truth and perseverance, fighting for a better future for our family.

To my mother, Patricia *(in memoriam)*, my queen and first true love, words cannot measure the depth of my gratitude for you, and I doubt they ever will. You witnessed the beginning of this journey, but sadly, not its conclusion. I dedicate all this work to you, as you were my greatest supporter, especially when no one else could be. You were always by my side, fighting every battle for me when I could not, and more importantly, teaching me how to fight these battles myself, enabling me to overcome every challenge that came my way. Since my birth, you embodied sweetness and love, and were also the best teacher I could possibly ask for. God now has His fierce angel by His side.

To my sister, Milena, I thank you for your companionship and support throughout my life, and for being my role model, as I strive to be yours.

I now dedicate this paragraph to my true love and life partner, my wife, Beatriz. Of all the people in my life, you are the one who truly knows me, understands my weaknesses and strengths, and comprehends my emotional states in every possible aspect. I cannot thank God enough for bringing you into my life, as you care for me every single day. None of this would be possible without your unwavering support and partnership. I am filled with gratitude every day when I pause to reflect on the fact that God has blessed me with such a precious gem of a person, far beyond anything I could have ever imagined. You are my heroine, and you must know that everything I do, I do for you and our family.

I would like to express my immense gratitude to my supervisor, Prof. Jorge Ricardo Mejia Salazar, for always championing my ideas and projects, striving within his limits to make everything possible and real. I remember all of our discussions, and you must know that you have left an indelible mark on my life with all of your teachings. I have become skilled in this field thanks to your guidance and support. You have shaped my career, and I hope we can continue to collaborate on many more studies in the future.

Additionally, I would like to extend my heartfelt thanks to our institution, the National Institute of Telecommunications (Inatel), for providing me with every opportu-

nity to expand my knowledge and advance my career path, from the beginning of my undergraduate studies in 2014 to the completion of this Master's degree.

Special thanks are due to Prof. Ashraf Uz Zaman from Chalmers University of Technology in Sweden, who essentially acted as my co-supervisor. His teaching and guidance have been instrumental in helping me become a better specialist in the field. He facilitated the measurement of our prototype at Chalmers and consistently went above and beyond to support and make the project possible.

*Bruno Ferreira Gomes*

The authors gratefully acknowledge the partial financial support provided through the project XGM-AFCCT-2024-3-1-1, funded by the xGMobile–EMBRAPII–Inatel Competence Center on 5G and 6G Networks, with resources from the PPI IoT/Manufatura 4.0 under MCTI grant number 052/2023, signed with EMBRAPII. Additionally, the authors extend their gratitude for the financial support from the Brazilian agencies: the National Council for Scientific and Technological Development (CNPq) under grant 314671/2021-8, and FAPEMIG under grant APQ-05305-23.

# Index

**Index** x

**List of Figures** xiv

**List of Tables** xv

**List of Abbreviations and Acronyms** xvii

**List of Symbols** xix

**Summary of Original Work** xxi

**Resumo** xxiii

**Abstract** xxv

**1 Introduction** 1

**2 Technical Background** 3
2.1 Introduction . . . 3
2.2 Fresnel Near Field Application Example . . . 6
2.3 Reactive Near Field Application example . . . 12
2.4 Feeding System Application Example . . . 16

**3 Chiral dielectric metasurfaces for broadband and highly integrable circularly polarized antenna** 19
3.1 Introduction . . . 19
3.2 Antenna Design . . . 20
3.2.1 Configuration . . . 20
3.2.2 Working principle and enhancement of ARBW . . . 21
3.3 Results and discussion . . . 22
3.4 Parametric Study . . . 25
3.5 Chapter Conclusions . . . 27

**4 Integrated Wideband Dual-Polarized ME-Dipole Planar Antenna Array with Tight Coupled Elements** 29
4.1 Introduction . . . 29

4.2 The ME-Dipole Concept . . . . . 30
4.3 Antenna Structure . . . . . 31
4.3.1 Element Design . . . . . 31
4.3.2 Radiator Operating Mechanism . . . . . 32
4.3.3 Dual Layer Feeding Mechanism . . . . . 33
4.3.4 $4 \times 4$ Planar Array . . . . . 33
4.4 Simulation . . . . . 34
4.5 Chapter Conclusions . . . . . 35

**5 All-Metallic-Metasurface-Based Wideband Dual Fabry-Perot Resonance Antenna Array with High Directivity and Polarization Purity 37**
5.1 Introduction . . . . . 37
5.2 Antenna Element Design . . . . . 39
5.2.1 Concept . . . . . 39
5.2.2 Integrated Gap-Waveguide Parallel Plate Design . . . . . 43
5.2.3 Simulated Results . . . . . 44
5.3 4x4 Antenna Array Design . . . . . 47
5.3.1 Feeding Network . . . . . 47
5.3.2 Prototype . . . . . 50
5.4 Simulation and Measurements . . . . . 51
5.5 Comparison with the State-of-the-Art Design Concepts . . . . . 52
5.6 Chapter Conclusions . . . . . 53

**6 Conclusions and Future Work 55**

**References 57**

# List of Figures


2.1 Presenting classification of the metamaterials accordingly to its electric permittivity and magnetic permeability values. Adapted from [1]. . . . . 4
2.2 Demonstration of the antenna scattering regions. . . . . 5
2.3 Overview on the feeding antenna system designed to elaborate the basic study for this thesis. . . . . 6
2.4 Overview on the classic figure of merits to evaluate the antenna performance. . . . . 7
2.5 Overview of the adapted structure proposed in the reference, with the achieved results. . . . . 8
2.6 Perspective demonstration of the source antenna integrated with the metasurface and a closer view on the 1x7 metasurface arrangement. . 9
2.7 Overview of the achieved results from the analysis for the metasurface composed of $1 \times 7$ array, with different distances to the source antenna. a) reflection coefficient, b) boresight directivity, c) Azimuth HPBW, d) Elevation HPBW, e) azimuth-plane directivity diagram at 14GHz and f) elevation-plane directivity diagram at 14GHz. . . . . 9
2.8 Perspective demonstration of the source antenna integrated with the metasurface in three diferent stages, first with one 1x7 metasurface above, followed by the stack up of two 1x7 metasurfaces, and finally three 1x7 metasurfaces. . . . . 10
2.9 Overview of the achieved results from the analysis for the metasurface related to each step of previous figure. Each sub-graph is defined as in 2.7. . . . . 11
2.10 Overview of the mushroom-like structure used in this study, accompanied of the dispersion diagram results for evaluation. . . . . 13
2.11 Overview of the integration between the source antenna and the mushroom-like structure. . . . . 14
2.12 Results for the reflection coefficient and the real and imaginary impedance parts for the integrated structure studied. . . . . 15
2.13 Study of the radiation pattern for all modes accepted by the metasurface. 15
2.14 Demonstration of the common ridge rectangular waveguide and the metasurface modified parallel-plate, named ridge-gap-waveguide. . . 17
2.15 Periodic pin geometry description and results of the modal allowance evaluation inside of the dispersion engineered structure. . . . . 17

2.16 Demonstration of the usage of the RGWG in a transition from a rectangular waveguide, highlighting the results and the E-field distribution. . . . . 18

3.1 3D geometric view of the proposed antenna element fed by a SIW ideal connector. . . . . 21
3.2 (a) Parametric side view of the antenna layers divided as: (b) SIW-to-coax feeding, (c) driven patch layer and (d) chiral dielectric metasurface layer. The design parameters are $x_1 = 10$ mm, $d = 10$ mm, $d_2 = 7.5$ mm, $p_{\text{len}} = 2.15$ mm, $d_{\text{via}} = 0.3$ mm, $d_{\text{pin}} = 0.4$ mm, $dist_{\text{via}} = 0.19$ mm, $d_1 = 5.71$ mm, $t_{\text{size}} = 0.86$ mm, $sp = 3.3$ mm, $l_f = 0.85$ mm, $w_f = 0.8$ mm, $ls = 2.1$ mm, $hs = 0.8$ mm, $\alpha = 60°$ and $\theta = 45°$. . . . . 22
3.3 Numerical results for (a) $S_{11}$ and (b) AR and boresight gain. Solid and dashed lines are for the patch antenna with and without (W/O) the DR metasurface. Simulations were carried out using the commercial software CST Studio. Horizontal dashed lines in (b) are eye guides for $AR = 3$ dB and boresight gain=8 dB. . . . . 23
3.4 Numerical results for $S_{11}$, AR and boresight gain are presented for the CDM-based antenna (a)-(b) with and (c)-(d) without the metal cavity. Simulations from CST Studio and ANSYS HFSS are indicated by solid and dashed lines. Horizontal dashed lines in (b) and (d) are eye guides for $AR = 3$ dB and boresight gain=8 dB. . . . . 23
3.5 Simulated **E**-field of the antenna element at orthogonal phases for both CP modes and both planes: Patch and DR Metasurface Planes. . . . . 24
3.6 Simulated radiation patterns at 27.5 GHz and 30 GHz for both cut-planes. 25
3.7 Simulated parametric study for reflection coefficient of the proposed antenna. (a) variation of $\theta$, (b) variation of $d_{cylinder}$, (c) variation of $ls$ and (d) variation of $dy_c$. . . . . 26
3.8 Simulated parametric study for AR of the proposed antenna. The variation of (a) $\theta$, (b) $d_{cylinder}$, (c) $ls$ and (d) $dy_c$ was the same as in Figures 3.7(a)-(d), respectively. . . . . 26

4.1 Principle of generating the ME-dipole response from a structure perspective. Adapted from [2] . . . . . 30
4.2 Demonstration of the ME-dipole background conceptualization. Adapted from [3] . . . . . 31
4.3 Schematic representation of the proposed antenna design. . . . . 31
4.4 Side-view of the antenna shown in Fig. 4.3, used to point out the feeding layers and other building elements. . . . . 32
4.5 Radiation mechanism description from the shared aperture concept. . 33
4.6 V-pol and H-pol feeding networks using the modified inverted microstrip gap waveguide. . . . . 34
4.7 Pictorial representation of the $4 \times 4$ planar array antenna design. . . . 34
4.8 $|S|$-parameters for the $4 \times 4$ planar antenna array. $|S_{11}|$ and $|S_{22}|$ are the reflection coefficients for V-pol and H-pol input ports, respectively, and $|S_{12}|$ represents the coupling between the V-pol and H-pol ports. . 35

4.9 Radiation patterns for both cut planes when fed by the V-pol input port. 35
4.10 Radiation patterns for both cut planes when fed by the H-pol input port. 36

5.1 Pictorial depiction of TEM and TE modes in the systems without (top panel) and with (bottom panel) metasurfaces. . . . . 39
5.2 (a) Schematic representation of a unit cell of the PEC-PMC cavity and (b) the corresponding PBG profile. . . . . 40
5.3 (a) Illustrative representation of the unit cell of a metasurface-based cavity and (b) the corresponding PBS. . . . . 40
5.4 Depiction of the TE (top panel) and TEM (bottom panel) feeding modes in the systems without (left-hand side) and with (right-hand side) metasurfaces. . . . . 41
5.5 Results are shown for the system a) without and b) with the bed of pins. Solid and dashed lines are for the TEM and TE ports, respectively. The insets in (a) and (b) are used to indicate that black, blue, red, and orange curves are for $d = 10$ mm, $d = 10.5$ mm, $d = 11$ mm, and $d = 11.5$ mm, respectively. . . . . 42
5.6 Far-field radiation patterns for (a)-(b) TE and (c)-(d) TEM modes. Data is comparatively presented for the antenna with pins in (a) and (c), and without pins in (b) and (d). Simulations were carried out for frequencies ranging from 12 GHz to 16 GHz, as shown in the insets. . 42
5.7 (a) Successive steps to prototype the antenna in this work: 1) a cavity back slotted (CBS) radiator; 2) CBS + parallel plates resonator; 3) CBS + parallel plates resonator with pins on one side; 4) CBS + parallel plates resonator with pins on both sides. Numerical results from full-wave electromagnetic simulations are shown for the (b) S-Parameters and (b) Boresight gain associated to each one of the prototyping steps in (a). . . . . 43
5.8 Parametric view of the antenna radiating element. The design parameters are $RGW_{\mathrm{p_pin}} = 4.5$ mm, $RGW_{\mathrm{a_pin}} = 2$ mm, $RGW_{\mathrm{w}} = 4$ mm, $RGW_{\mathrm{c}} = 8$ mm, $slot_{\mathrm{w}} = 17$ mm, $slot_{\mathrm{s}} = 9$ mm, $PP_{\mathrm{dist}} = 10.5$ mm, $a_{\mathrm{pin}} = 2.2$ mm, $p_{\mathrm{pin}} = 4.9$ mm, $UC_{\mathrm{l}} = 23.5$ mm, $PP_{\mathrm{l}} = 16$ mm, $RGW_{\mathrm{h}} = 7$ mm, $PP_{\mathrm{pin_h}} = 3$ mm, $Pin_{\mathrm{Gap_PP}} = 4.5$ mm and $RGW_{\mathrm{Pin_h}} = 6$. . . . . 43
5.9 Numerical results illustrating the variation of the electric field distribution across multiple observation planes within the specified frequency band. Each plane offers a detailed view of how the electric field changes at different positions, providing significant insights into the field's behavior and characteristics over the frequency range. . . . . 45
5.10 (a) Description of the simulated element boundary conditions and (b) the related reflection coefficient results under each circumstance. . . . 46
5.11 Overview on some radiation pattern figure-of-merit evolution aligned to each applied boundary conditions in the simulated element. . . . . 46

5.12 Viewing of external and internal designed antenna model comprising radiation and signal layers. On left side, the 3D model of the full 4x4 proposed array and on right side, the signal distribution portraying the designed power dividers . . . . . 48
5.13 Simulated results from the transitions required on the design to enable a measuring interface for the prototype antenna model. . . . . 48
5.14 Reflection coefficient simulated results for the different designed power dividers located in the GW signal layer. . . . . 49
5.15 Prototype viewing of the proposed antenna. Top view with the radiation aperture and 3D-view in the anechoic chamber ready for measurements. . . . . 50
5.16 Demonstration of the situational concern in regards of the mounting method of the prototype, related to the divergence in the measured parameters. . . . . 51
5.17 Comparison between simulated and measured S-parameters and Realized Boresight Gain of the proposed antenna concept. . . . . 51
5.18 Comparison between simulated and measured radiation patterns for both farfield cut sections: azimuth and elevation, demonstrated at different frequency points. . . . . 52

# List of Tables

3.1 Performance Comparison among CP Antennas . . . . . 27

5.1 Performance Comparison among Metal Antennas with GW feeding network . . . . . 52
5.2 Performance Comparison among Metantennas . . . . . 52

# List of Abbreviations and Acronyms

| | |
|---|---|
| 5G | fifth generation of mobile communications |
| A-HPBW | azimuth half power beamwidth |
| AESA | active electronically scanned array |
| AR | axial ratio |
| BW | bandwidth |
| CBS | cavity-backed slot |
| CDM | chiral dielectric metasurface |
| CMR | common mode resonance |
| CNC | computer numerical control |
| CP | circularly polarized |
| CPR | co-cross polarization ratio |
| DNG | double-negative |
| DPS | double-positive |
| DRA | dielectric resonator antenna |
| E-HPBW | elevation half power beamwidth |
| ENZ | epsilon-near-zero |
| FEM | finite element method |
| FIT | finite integration technique |
| FPR | febry-perot resonator |
| GND | ground plane |
| GW | gap waveguide |
| H-pol | horizontal polarization |
| LCP | left circularly polarized |
| ME | magneto-electric |
| mmWave | millimiter wave |
| MNZ | mu-near-zero |
| OB | open boundary |
| PB | periodic boundary |
| PBG | photonic bandgap |
| PBS | photonic band structure |
| PCB | printed circuit board |
| PEC | perfect electric conductor |
| PMC | perfect magnetic conductor |
| PP | parallel plate |
| RCP | right circularly polarized |
| RGW | ridge gap waveguide |

| | |
|---|---|
| SIW | substrate integrated waveguide |
| SLL | side lobe level |
| TE | transverse electric |
| TEM | transverse electromagnetic |
| TM | transverse magnetic |
| UWB | ultra wideband |
| V-pol | vertical polarization |
| VSWR | voltage standing wave ratio |

# List of Symbols

| | |
|---|---|
| $\beta$ | wave factor |
| $\epsilon$ | media dielectric permitivitty |
| $\epsilon_{\mathrm{r}}$ | relative material permittivity |
| $\epsilon_{\circ}$ | vacuum dielectric permittivity |
| $\tan\delta$ | loss tangent |
| $\tilde{\alpha}$ | complex electric polarizability |
| $\tilde{\chi}$ | complex magnetic polarizability |
| $\tilde{B}$ | complex magnetic field |
| $\tilde{E}$ | complex electric field |
| $\tilde{G}$ | electric-magnetic dipole polarizability |
| $\tilde{m}$ | magnetic dipole |
| $\tilde{p}$ | electric dipole |
| $c$ | speed of light in vacuum |
| $n$ | mode number |

# Summary of Original Work

- **Ferreira-Gomes, B.**; Oliveira, O.N., Jr.; Mejía-Salazar, J.R. "Chiral Dielectric Metasurfaces for Highly Integrated, Broadband Circularly Polarized Antenna," *Sensors* **2021**, 21, 2071.
- **B. F. Gomes** and J. R. Mejía-Salazar, "Integrated Wideband Dual-Polarized ME-Dipole Planar Antenna Array with Tight Coupled Elements," *2022 16th European Conference on Antennas and Propagation (EuCAP)*, Madrid, Spain, **2022**, pp. 1-4.

# Resumo

Gomes, B.F. On the Metasurface Integration and Design for Wave Manipulation Improvement of Antenna Systems [Master's Thesis]. Santa Rita do Sapucaí: Instituto Nacional de Telecomunicações; 2024.

Esta dissertação de mestrado explora a combinação de metamateriais e metasuperfícies com designs de antenas para gerar mecanismos radiantes modificados através da manipulação inteligente de ondas. Integrando metasuperfícies em vários pontos dentro da antena, demonstramos como esses materiais artificiais podem ser ajustados e sintonizados para resolver deficiências específicas para aplicações direcionadas. A tese começa com uma visão geral dos fundamentos teóricos e princípios dos metamateriais e metasuperfícies, proporcionando uma sólida base técnica. Em seguida, discute o uso de uma metasuperfície quiral para melhorar a radiação de ondas circularmente polarizadas, destacando melhorias na largura de banda de polarização e no coeficiente de reflexão, com resultados de simulação indicando larguras de banda de correspondência de impedância de até 22.6% ($25.3 - 31.6$ GHz) com larguras de banda de AR de 3-dB de 11.6% ($26.9 - 30.2$ GHz), enquanto em termos de compacidade poderia proporcionar ($0.95\lambda_0 \times 0.95\lambda_0$). Em seguida, a implementação de um dipolo magneto-elétrico de abertura compartilhada com uma rede de alimentação de guia de onda com fenda modificada é usada para alcançar uma antena de matriz escalável de banda ultra larga (UWB) de dupla polarização, abordando os desafios e soluções para integrar esquemas de dupla polarização dentro de um dipolo compacto de abertura compartilhada, apresentando resultados numéricos com largura de banda de impedância de 68.6%(16.1 GHz-32.9 GHz) para a polarização vertical e 73.3%(15.2 GHz-32.8 GHz) para a polarização horizontal, considerando um VSWR (relação de onda estacionária de tensão)$<$2. Finalmente, a tese apresenta demonstrações numéricas e experimentais de uma matriz de antenas 4x4, destacando como um conceito baseado em metasuperfície em antenas de cavidade de placa paralela convencional pode melhorar significativamente a largura de banda, manter altos níveis de ganho e garantir uma polarização de alta pureza no feixe irradiado, com largura de banda de impedância medida em torno de 21% (12 GHz-14.8 GHz) e ganho medido de até 22.9 dBi. Essas percepções abrangentes sobre o uso inovador de metasuperfícies no design de antenas demonstram melhorias significativas no desempenho e abrem caminho para futuras implementações práticas.

***Palavras-Chave*:** Metamateriais, Metasuperfícies, Metantenas, Arranjo de Antenas, Diagrama de Radiação, Manipulação de Ondas.

# Abstract

Gomes, B.F. On the Metasurface Integration and Design for Wave Manipulation Improvement of Antenna Systems [Master's Thesis]. Santa Rita do Sapucaí: Instituto Nacional de Telecomunicações; 2024.

This master's dissertation explores the combination of metamaterials and metasurfaces with antenna designs to generate modified radiating mechanisms through smart wave manipulation. By integrating metasurfaces at various points within the antenna, we demonstrate how these artificial materials can be tailored and tuned to address specific drawbacks for targeted applications. The thesis begins with an overview of the theoretical foundations and principles of metamaterials and metasurfaces, providing a solid technical background. It then discusses the use of a chiral metasurface to improve the radiation of circularly polarized waves, highlighting enhancements in polarization bandwidth and reflection coefficient, with simulation results indicating impedance-matching bandwidths up to 22.6% ($25.3 - 31.6$ GHz) with 3-dB AR bandwidths of 11.6% ($26.9 - 30.2$ GHz), while in terms of compactness could provide ($0.95\lambda_0 \times 0.95\lambda_0$). Next, the implementation of a shared aperture magneto-electric dipole with a modified gap waveguide feeding network is used to achieve an ultra-wideband (UWB) dual-polarized scalable antenna array, addressing the challenges and solutions for integrating dual-polarized schemes within a shared aperture tight dipole, presenting numerical results with impedance bandwidth of 68.6%(16.1 GHz-32.9 GHz) for the vertical polarization and 73.3%(15.2 GHz-32.8 GHz) for horizontal polarization, considering a VSWR (voltage standing wave ratio)$<$2. Finally, the thesis presents numerical and experimental demonstrations of a 4x4 antenna array, featuring how a metasurface-based concept in conventional parallel plate cavity antennas can significantly improve bandwidth, maintain high gain levels, and ensure high-purity polarization in the radiated beam, with measured impedance bandwidth around 21% (12 GHz-14.8 GHz) and measured gain of up to 22.9 dBi. These comprehensive insights into the innovative use of metasurfaces in antenna design showcase significant performance improvements and pave the way for future practical implementations.

***Keywords*:** Metamaterials, Metasurfaces, Metantennas, Antenna Array, Radiation Pattern, Wave Manipulation.

# Chapter 1

# Introduction

In the realm of wireless communication and sensing technologies, there has been a surge in demand for high-performance antennas [4]. Among these, Ultrawideband (UWB) antennas have gained prominence due to their versatility in both military and civilian applications, ranging from high data-rate communications to advanced imaging systems [4]. Despite their benefits, traditional UWB antennas face significant challenges, such as large sizes, limited bandwidth, and suboptimal aperture utilization. To address these drawbacks, one innovative solution is the Magneto-Electric (ME) dipole antenna. ME dipole antennas tackle constraints like profile height and front-to-back ratio by employing several advanced strategies. These include folding the magneto-dipole multiple times and integrating components such as exponential-folded plates, U-shaped reflectors, and wave-director plates. Consequently, the ME dipole antenna achieves a more compact design, reduced profile height, and enhanced aperture efficiency [5]. Another effective strategy to enhance antenna performance involves organizing isolated elements into arrays. Antenna arrays are renowned for their high directivity and gain, playing crucial roles in communications, radar systems, and electronic warfare [6]. Among these, phased array antennas are particularly notable for their electronic scanning capabilities, which allow for dynamic control over the shape and direction of the radiation pattern. The pursuit of higher bandwidth and performance has propelled UWB phased array antennas into the spotlight. These antenna arrays are essential components for systems like 5G (the fifth generation of mobile communications), delivering wide bandwidth, high gain, and broad scanning capabilities. Nevertheless, designing UWB phased array antennas presents unique challenges that need to be overcome, including the rejection of grating lobes, management of mutual coupling, minimization of gain fluctuations, and generation of multiple beams [4].

Recent efforts to tackle these challenges have centered on integrating metamaterials and metasurfaces into antenna design [7]. Emerging in the late 20th century, metamaterials signify a major breakthrough in artificial materials. Electromagnetic (EM) metamaterials, in particular, consist of sub-wavelength scatterers that offer unparalleled abilities to manipulate electromagnetic wave propagation, effectively addressing the limitations of natural materials [8]. Recent efforts to tackle these challenges have centered on integrating metamaterials and metasurfaces into antenna design [7]. Emerging in the late 20th century, metamaterials signify a major breakthrough in artificial ma-

terials. Electromagnetic (EM) metamaterials, in particular, consist of sub-wavelength scatterers that offer unparalleled abilities to manipulate electromagnetic wave propagation, effectively addressing the limitations of natural materials [8]. Metamaterials with thicknesses less than the operating wavelength exhibit two-dimensional (2D) features, commonly known as metasurfaces. These metasurfaces enable versatile functions such as frequency selection, polarization conversion, and beam steering. When integrated with antennas, metasurfaces can significantly enhance gain, bandwidth, and aperture efficiency. Though initially utilized as auxiliary components in antenna design, metasurfaces have evolved to become integral elements of modern antenna architectures. This progression has culminated in the development of metantennas, where metasurfaces function as the primary radiating aperture [8].

In this master's thesis, we delve into the use of metasurfaces for designing antennas. Chapter 2 explores the application of antennas in the near-field and reactive near-field, as well as their role in the feeding system. In Chapter 3, we demonstrate how all-dielectric metasurfaces can be used as the radiating element of an antenna to improve the bandwidth and performance of circularly polarized antennas and antenna arrays, thus providing various benefits to the proposed concept. Chapter 4 highlights the use of ME dipole antenna design in a dual-polarized configuration, pushing the boundaries of ultra-wideband (UWB) phased array antenna technology. The implementation of metasurfaces within the antenna radiating aperture is discussed in Chapter 5. We demonstrate that this latter approach offers wideband performance, a highly directive pattern, and high polarization purity, among other advantages. Additionally, we explore the benefits of an arrayed solution, which is further manufactured and measured, showcasing the stability and feasibility of the proposed design.

Finally, contributions from this work to the international scientific literature are listed below:

- Bruno Ferreira-Gomes, Ashraf Uz Zaman, and J. R. Mejía-Salazar, 'All-Metallic-Metasurface-Based Wideband Dual Fabry-Perot Resonance Antenna Array with High Directivity and Polarization Purity", *under review*.
- Bruno Ferreira-Gomes and J. R. Mejía-Salazar, "Integrated Wideband Dual-Polarized ME-Dipole Planar Antenna Array with Tight Coupled Elements", EuCAP 2022, DOI: 10.23919/EuCAP53622.2022.9769240
- Bruno Ferreira-Gomes, O. N. Oliveira Jr, and J. R. Mejía-Salazar, "Chiral Dielectric Metasurfaces for Highly Integrated, Broadband Circularly Polarized Antenna", Sensors 2071, 21 (2021).

# Chapter 2

# Technical Background

## 2.1 Introduction

We begin this chapter with a rapid overview of the history of metamaterials. The concept was first theoretically studied by Victor Veselago, a Russian physicist and mathematician, who in 1968 proposed the possibility of achieving both negative permittivity and permeability in a material [9]. Veselago observed that under these specific conditions, a 180-degree phase rotation would occur in the Poynting vector (power flow) relative to the plane wave phase velocity. This phenomenon was derived from calculations using Maxwell's equations for such materials. Following Veselago's pioneering work, between 1998 and 1999, John Pendry, an English theoretical physicist, along with his colleagues, proposed the first practical structures that could partially alter the intrinsic media behavior to mimic that of a homogeneous material, thus affecting wave propagation. Their studies, published in 1998 and 1999 [10, 11], introduced an array of metallic pins to modify permittivity and magnetic resonators to modify permeability. In 2001, a significant advancement was made by a group of scientists –Shelby, Smith, and Schultz– who successfully created a structure that simultaneously exhibited negative permittivity and permeability. This achievement, which combined both of Pendry et al.'s proposals, empirically validated the behavior initially predicted by Veselago [12].

Metamaterials have captivated academia due to their wide-ranging applications in electromagnetics. In 2002, Enoch *et al.* introduced a groundbreaking concept by integrating metamaterials with antennas, forming what is known as a metasurface [13]. This involved stacking metamaterial unit cells above a monopole antenna to precisely control its radiation pattern. This innovation enabled focused radiation in desired directions, narrowing the beam and enhancing system directivity. Subsequent research has explored numerous antenna-metamaterial combinations for enhancing bandwidth, shaping radiation patterns, and achieving miniaturization. These metamaterials are often classified and represented in charts based on the signs of their permittivity and permeability, as illustrated in Figure 2.1. Materials exhibiting positive permittivity and permeability are typically categorized in the first quadrant, whereas those with negative values are placed in the third quadrant. Intermediate configurations, which either electric or magnetic fields become evanescent, are classified in the second and fourth

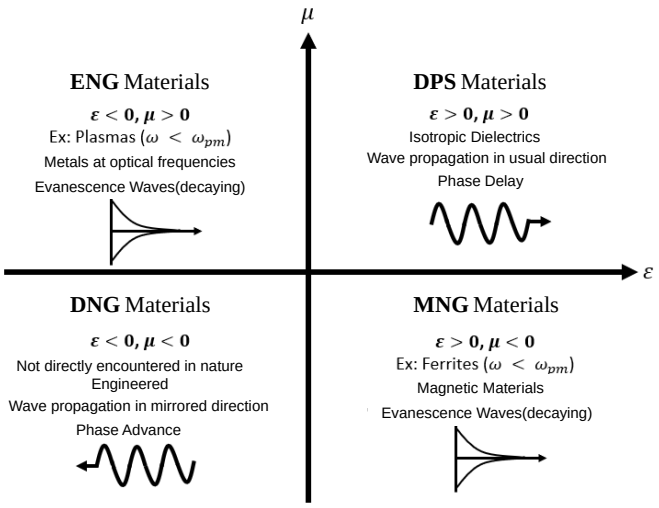



Figure 2.1: *Presenting classification of the metamaterials accordingly to its electric permittivity and magnetic permeability values. Adapted from [1].*

quadrants, respectively [1]. It is important to mention that once one field component becomes evanescent, the orthogonally related field component also becomes evanescent, resulting in an evanescent wave. This systematic classification aids researchers in understanding and selecting metamaterial designs tailored for specific electromagnetic applications.

In the context of antennas, metamaterials and/or metasurfaces should be tailored and tuned according to the specific component of the antenna that needs enhancement. Therefore, it is essential to first discuss the electromagnetic behavior in both the near-field and far-field regions. Furthermore, the near-field zone can be divided into two significant sections, named the reactive near-field zone and the radiative Fresnel near-field zone. This division is illustrated in Figure 2.2, where the far-field region is also depicted for didactic purposes. By understanding the distinct characteristics of these regions, we can effectively design and optimize metamaterials and metasurfaces for improved antenna performance.

The explanation here begins with the reactive near field, where the radiating characteristics of the antenna are highly susceptible to modification by surrounding structures. This region serves as the foundational area for the radiating model, with all surrounding elements contributing to the creation and maintenance of the antenna's field performance. This interaction significantly influences how the antenna will radiate to the far-field [6]. Typically, the reactive near field is defined as being close to the antenna, with its limits approximately $\frac{\lambda}{6}$ away from the antenna's surface. While this definition can be used for general purposes, a more precise definition is required for specific designs. Figure 2.2 illustrates that a more appropriate model must consider both the wavelength ($\lambda$) and the largest dimension of the radiating antenna aperture ($D$). Through these features, we observe that any modifications in the reactive near field must be integrated with the antenna source as a single component to ensure effective performance.

The Fresnel zone, on the other hand, is a region where controlled modifications

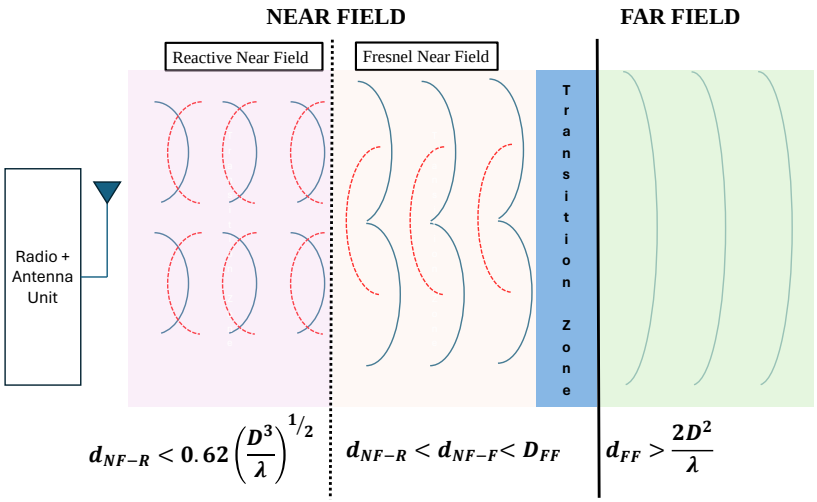



Figure 2.2: *Demonstration of the antenna scattering regions.*

can be performed without directly affecting the radiating characteristics of the source antenna, provided the modifications are designed appropriately [6]. In this zone, the returning wave strength is reduced, allowing for greater freedom in engineering the surrounding structures without immediate dependencies on the source antenna. In practical terms, the source antenna and the near field area can initially be decoupled. After making the necessary modifications, they can be recombined to investigate further effects of interest. Typically, the outer limits of the Fresnel zone range from approximately $\frac{\lambda}{4}$ to $\lambda$ away from the source antenna. For better accuracy and consistency, the formulas presented in Figure 2.2 should be used to define these boundaries.

The transition zone, illustrated in Figure 2.2, is often less discussed because it is essentially part of the near-field region. However, this zone is crucial as it marks the transition towards the stability expected in the far-field region. In this zone, the radiated wave first becomes balanced, achieving the correct proportionality between the electric and magnetic fields for effective propagation [6]. To quantify, the transition zone typically begins at a distance of around $\lambda$ from the source antenna and ends where the far-field or the same source begins, as calculated by the formula in Figure 2.2. The far-field region is characterized by the absence of returning waves reaching the source, and the radiated spherical wave exhibits dipole features with either transverse electric or transverse magnetic fields [6]. As the wave propagates away from the source in the far-field, the radiated energy spreads over a vast spherical surface area.

Having discussed these foundational topics, we will now present simulations to demonstrate how metamaterials and metasurfaces can be utilized in the previously discussed field regions of the antenna. This initial study will provide us with an understanding of how each field region of an antenna, and its general performance, is affected by the use of metasurfaces. We will start with the Fresnel near-field application example, as manipulation in this area is simpler, making it a good starting point for didactic purposes. We will then proceed to the reactive near-field with a more complex demonstration, and finally, we will analyze the application of metamaterials to a feeding system, which is not a component of the radiating area, differing from the previous cases.

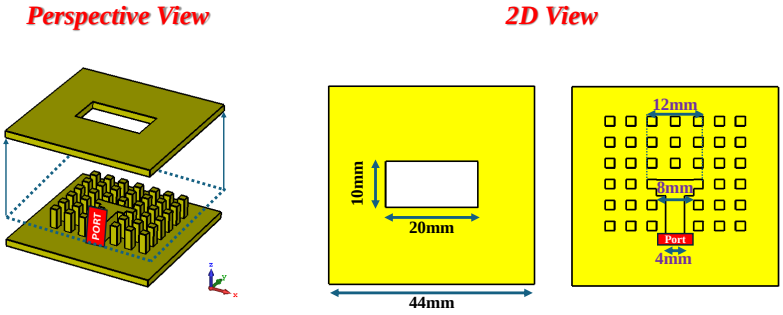



Figure 2.3: *Overview on the feeding antenna system designed to elaborate the basic study for this thesis.*

## 2.2 Fresnel Near Field Application Example

To begin our study, we examine a simple cavity-backed slot antenna model designed to operate between 11.5 GHz and 14.5 GHz. The antenna is fed ideally with a ridge gap waveguide, detailed further in the section titled "Feeding System Application Example". Our primary focus is to evaluate the performance of this basic antenna and understand how its characteristics change when metamaterials are introduced near its surface. Figure 2.3 illustrates the conceptual design used in this study, providing a comprehensive view of its configuration. The top plate has been lifted to reveal the underlying layers for clarity. Geometric dimensions are included for illustrative purposes, emphasizing that the goal here is not to teach antenna design but rather to analyze the antenna's performance before and after incorporating metamaterial concepts. Figure 2.4 presents key performance parameters of the slot antenna. From top left to bottom left, these parameters include the reflection coefficient, boresight directivity, and half-power beamwidths (HPBW) for both elevation and azimuth planes. We should remark here that the radiation pattern diagram was determined based on the polarization direction of the slot antenna, which aligns with the current around the slot edges oscillating along the $x$-axis, as defined in Figure 2.3. Consequently, this axis becomes the azimuth observation plane, while the cross-polarization component corresponds to the elevation observation plane. In this design, the reflection coefficient is optimized to achieve at least -10 dB across the specified frequency bandwidth, ensuring effective radiation with minimal reflection back to the source. On the right side of Figure 2.4, radiation patterns are plotted at three matched frequency points: 12 GHz, 13 GHz, and 14 GHz, for both elevation ($\phi = 90°$) and azimuth ($\phi = 0°$) cases. These patterns provide insights into the boresight gain and HPBWs after post-processing.

With a clear understanding of the antenna's design and performance characteristics, we move forward to explore the impact of introducing a metamaterial component into the Fresnel near-field region. The basic proposed antenna is referred in this project from now on as *source antenna*, representing the active radiator, as the main source of radiation for the system studied. This section draws inspiration from the Ref. [14], scaled down to operate within our slot antenna's frequency range. The metamaterial unit cell is designed to exhibit a narrow bandwidth resonance with negative permeabil-

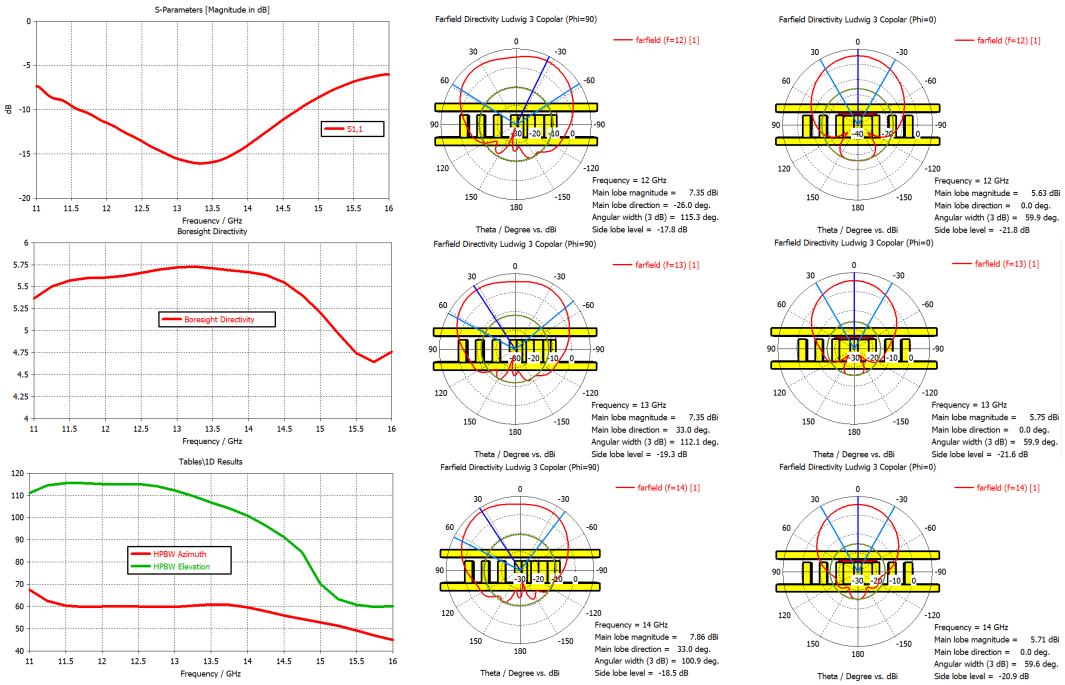



Figure 2.4: *Overview on the classic figure of merits to evaluate the antenna performance.*

ity, followed by lower permeability levels. This behavior facilitates the manipulation of coupled currents, allowing for the creation of a metasurface lens composed of multiple unit cells. In the referenced paper, the authors used a planar printed wideband bow-tie dipole antenna with end-fire radiation and pure linear polarization along the dipole axis. Our antenna, however, radiates in the boresight direction, necessitating alignment of the linear polarization with the metasurface lens. Figure 2.5 demonstrates the metamaterial unit cell evaluated in our study and its response when excited by a uniform plane wave with linear polarization aligned to the antenna's polarization axis. The results indicate that while our extracted parameters did not achieve negative permeability resonance as expected, they demonstrate similar effects observed as in [14]. Moreover, the permittivity could also be effectively manipulated within a certain bandwidth, significantly lowering the refractive index. It's important to note that post-processing algorithms and material properties can influence simulation results, leading to slight variations in negative values observed, although overall consistency is maintained.

The next step in this study is to include then, the metamaterial array over the slot antenna source. To follow this, the array was then composed of seven resonating structures denominated 1x7 array, and the study was carried out by varying the distance to the source, and also applying the 1x7 array configuration along the propagation direction to study its effects. The same antenna figure of merit parameters will be compared to make sure the effect is understood. In figure 2.6 it can be seen how the metasurface placement is organized above the source antenna and the parameter modified to generate the results. It can be also seen how the metasurface arrangement is designed to achieve this previous mentioned 1x7 array. For demonstration purpose, the parameter $Surface_{Dist}$ was evaluated only at two different points, numbered 5mm and 10mm, related to quarter wavelength ($\frac{\lambda}{4}$) and half wavelength ($\frac{\lambda}{2}$) at 14GHz, demonstrating

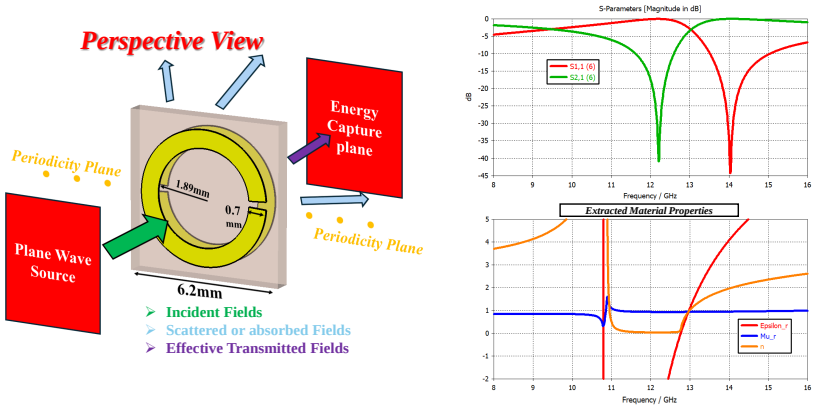



Figure 2.5: *Overview of the adapted structure proposed in the reference, with the achieved results.*

how the structures are seen in the Fresnel near-field zone. In figure 2.7, it can be noted all the achieved results compared to the standalone source antenna. To summarize the data:

- **a)** It can be noticed that the behavior of the reflection coefficient is not changing that much in regards of the standalone source antenna, and this comes from the Fresnel near-field zone study, which showed that within this zone, a small part of the waves are reflected back to the source, causing some variation to happen. It can be seen that, further we get from the source, the wave reflections get further reduced, then, not even changing the bandwidth of the source antenna, while closer to it, move reflection caused the matching to shift in frequency, with a small reduction in the bandwidth.
- **b)** The addition of the first layer of the metalens demonstrated that the directivity of the source antenna could be improved with the combination proposed. Here, the closer the parasitic was to the source antenna, the directivity increase was around 1dB for most of the bandwidth and that when it was spaced a bit more, this directivity benefit was focused more above 13GHz, which is the point in which the metamaterial refraction index is above 1. This demonstrates that there is a compromise between the placement of the metasurface, related to the expected simulated behaviour of the metamaterial proposed.
- **c)** and **d)** The HPBW over frequency for both elevation and azimuth planes are presented. This plot is used as a support to understand what is happening with the beam when this structure is around the source antenna. There is a really good compromise with the boresight directivity and the placement of the array along the linear polarization direction, demonstrating that the pattern is changing mostly in the azimuth plane, which is the direction in which the array is constructed. The elevation plane also gives the overview of what this beam shaping effect is capable of doing there.
- **e)** and **f)** For sake of plotting multiple diagrams, it was plotted it in the most interesting shared point, 14GHz, in which the effect is stronger for both separation scenarios. Here a better visualization of what happens to the pattern is observed.

The next phase of our study involves integrating a metamaterial array onto the slot

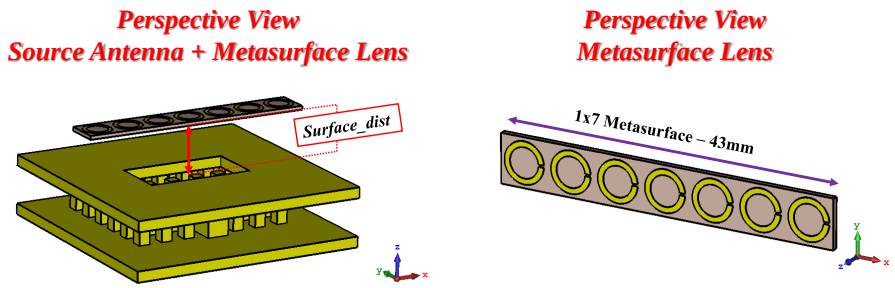



Figure 2.6: *Perspective demonstration of the source antenna integrated with the metasurface and a closer view on the 1x7 metasurface arrangement.*

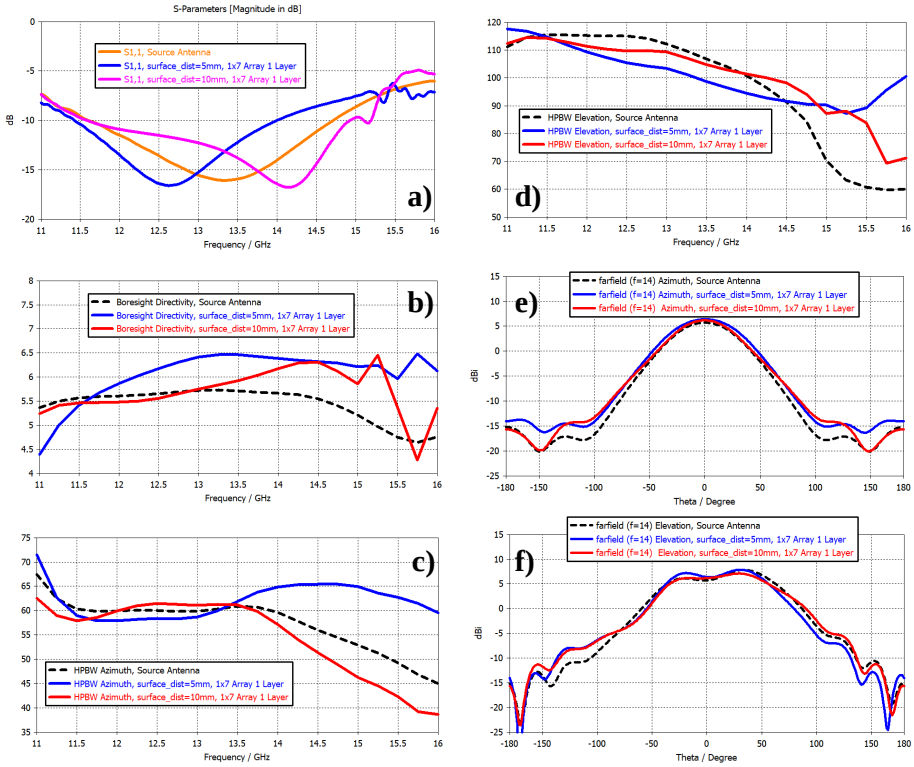



Figure 2.7: *Overview of the achieved results from the analysis for the metasurface composed of* $1 \times 7$ *array, with different distances to the source antenna. a) reflection coefficient, b) boresight directivity, c) Azimuth HPBW, d) Elevation HPBW, e) azimuth-plane directivity diagram at 14GHz and f) elevation-plane directivity diagram at 14GHz.*

antenna source. This $1 \times 7$ array comprises seven resonating structures strategically placed to investigate their effects on the antenna's performance. The array configuration is aligned along the propagation direction, and the study examines how varying the distance between the array and the source impacts key parameters. Figure 2.6 illustrates the arrangement of the metasurface above the source antenna and highlights the parameters adjusted during the study. Specifically, the parameter $Surface_{Dist}$ is eval-

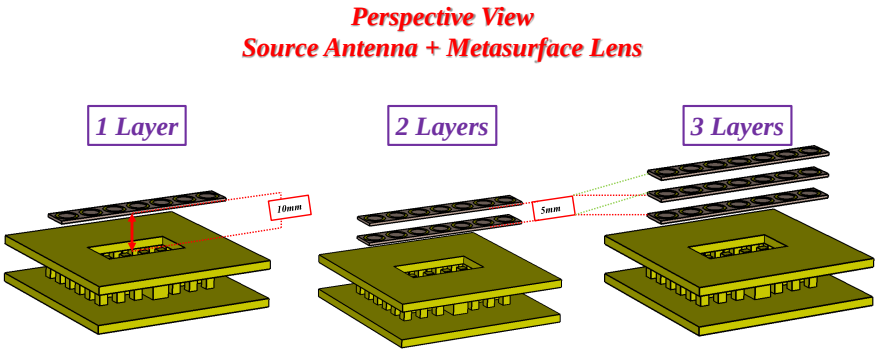



Figure 2.8: *Perspective demonstration of the source antenna integrated with the metasurface in three diferent stages, first with one 1x7 metasurface above, followed by the stack up of two 1x7 metasurfaces, and finally three 1x7 metasurfaces.*

uated at two points: 5mm and 10mm. These distances correspond to a quarter wavelength ($\frac{\lambda}{4}$) and half wavelength ($\frac{\lambda}{2}$) at 14 GHz, respectively, positioning them within the Fresnel near-field zone. To understand the enhancements achieved, we compare the antenna's performance with and without the metamaterial array. Figure 2.7 presents these comparative results, focusing on key parameters such as reflection coefficient, directivity, and beamwidth. Furthermore, we explore the effects of adding multiple metasurface layers to the antenna design. Figure 2.8 shows the inclusion of up to three metasurface layers, with corresponding numerical results detailed in Figures 2.9(a)-(f). These results sequentially reveal the impact of each additional layer on the antenna's performance, as discussed below (in relation to Figures 2.9(a)-(f)):

- **a)** The addition of the new layers spaced of $\frac{\lambda}{4}$ did not compromise so much the influence in the reflection coefficient. Basically, it can be noted that the reflected waves in these structures are further reduced as the layers are further spaced from the source antenna, causing less impacts when each layer is included.
- **b)** Here is where the majority of the influence can be observed. By stacking up more layers, it is definitively observed that the directivity of the design is improved. The addition of the first layer caused a less impact in this variance, causing the directivity to increase around 0.5dBi around 14GHz, while for the included second layer, this directivity improvement was around 2.4dBi also evaluated at the same frequency point. The second layer also caused a more broader bandwidth improvement, but with major response at 14GHz. When the third layer is included, a broader stable influence in the directivity is presented, with around 1.6dBi, causing the effect to influence most of the operation bandwith of the source antenna.
- **c)** and **d)** The HPBW over frequency for both elevation and azimuth planes are presented. The relation to the evaluated directivity change can be directly observed in these plots as well. Here it can be seen that the addition of the new layers are definitely beam shaping the diagrams, creating the intended lens effect, in which the second layer caused both the azimuth and elevation planes to change a lot when compared to the stand alone source antenna, while the third

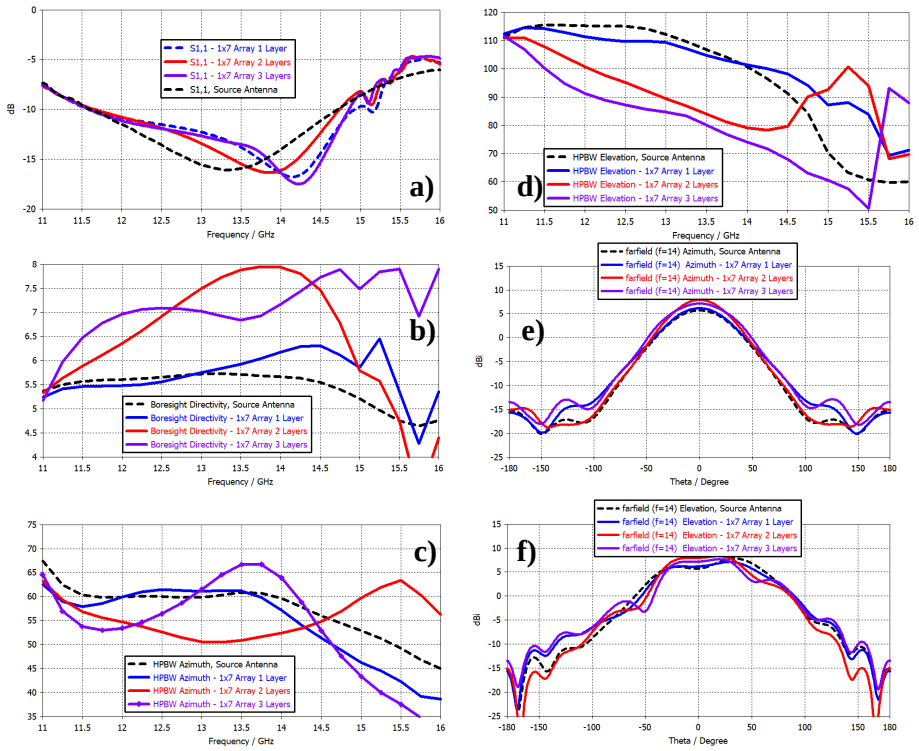



Figure 2.9: *Overview of the achieved results from the analysis for the metasurface related to each step of previous figure. Each sub-graph is defined as in 2.7.*

layer had its major effects in the change of the elevation diagrams. This demonstrates that the third layer is already capturing multiple cross polar fields from the environment and distorting along the orthogonal linear polarization radiated by the source antenna.

- **e)** and **f)** The fields are plotted again for 14GHz frequency point, so it can be observed how the diagrams in both azimuth and elevation are changing with proposed structure modifications. The linear polarization of the antenna keeps as it was, before adding the multi layer lens.

As it can be observed, most of the radiation pattern plots were used assuming Ludwig3 method. Despite there is no difference in the directivity calculation when compared to conventional calculation, after the polarization and the components of the fields are treated correctly, as it was done here, it is worth to mention the reason and the intention. The main difference between the conventional calculation of antenna directivity and the Ludwig3 model lies in how the electromagnetic field components are treated. The conventional method uses projections in spherical coordinates $E_\theta$ and $E_\phi$, whereas the Ludwig3 model transforms these components to account for copolarization and cross-polarization in a manner independent of the measurement plane orientation. This transformation allows for a more accurate analysis of directivity concerning polarization, making the Ludwig3 model particularly beneficial in applications where polarization is critical, such as in mobile communications and radar systems. In the case of this chapter, it is realistic to observe Ludwig3 method, so we can evaluate

how the metamaterial structures placed on the source antenna can alter the polarization of the new radiated pattern with accuracy.

In conclusion, this section has demonstrated one of several applications showcasing how metasurfaces integrated into the Fresnel near-field of antennas can effectively modify their characteristics through engineered wave manipulation solutions. The study highlighted the potential for enhancing antenna performance by strategically deploying metamaterials in this region. The next section will delve deeper into the use of engineered metasurfaces within the reactive near-field zone of a source antenna. This exploration will further expand on how such applications can optimize antenna functionality and performance in practical scenarios.

## 2.3 Reactive Near Field Application example

The reactive near-field zone, as described earlier, presents a complex scenario where any integrated parasitic component can significantly alter electromagnetic field effects to the extent that the source antenna and the parasitic element behave as a single entity. For instance, if a metal rod is introduced near the aperture of the source antenna, it is likely to cause a de-tuning of the original radiation, either disrupting or enhancing the radiation characteristics of the source antenna. Unless this rod is carefully modified to support and improve the original source antenna, the system may fail to function effectively with such a parasitic element near its aperture. In this scenario, the system becomes a single entity composed of both the source antenna and the rod, with each possessing the ability to modify the radiation behavior. This interaction will occur regardless of the structure used, as long as it can resonate within the observed frequency range. The ability to modify the reactive near field with parasitic components allows for antenna miniaturization, polarization modification, and significantly more advantageous system enhancements. Unlike the Fresnel near-field application discussed previously, where metasurfaces were placed above the source antenna with noticeable modifications in radiated parameters despite minimal changes in the antenna's original structure, the reactive near-field integration demands a unified optimization approach. Here, both the source antenna and the metasurface must be optimized together and in parallel to ensure effective system operation. In this section, the methodology is based on a study outlined in [15]. This study employs a metasurface array consisting of grounded pins with patches on top, forming a dispersion-engineered structure commonly referred to as a "mushroom shape". The authors utilize a slot radiator fed by a microstrip line, placing the mushroom-like metasurface above the radiating slot while sharing a common ground plane. The advantage lies in the engineered dispersion characteristics of the mushroom structure, which facilitates the excitation of the first $TE_{10}$ mode with zero and anti-phase $TE_{20}$ modes, achieving resonance points close to each other. This design approach enables bandwidth extension and low-profile configuration. The study provides empirical design guidelines to create such concepts, emphasizing the importance of understanding how these structures can be effectively implemented. Specifically, in the context of integrating metamaterials into the reactive near-field zone, the focus shifts towards exploring how these structures behave when higher-order modes are allowed to propagate alongside fundamental modes, as detailed

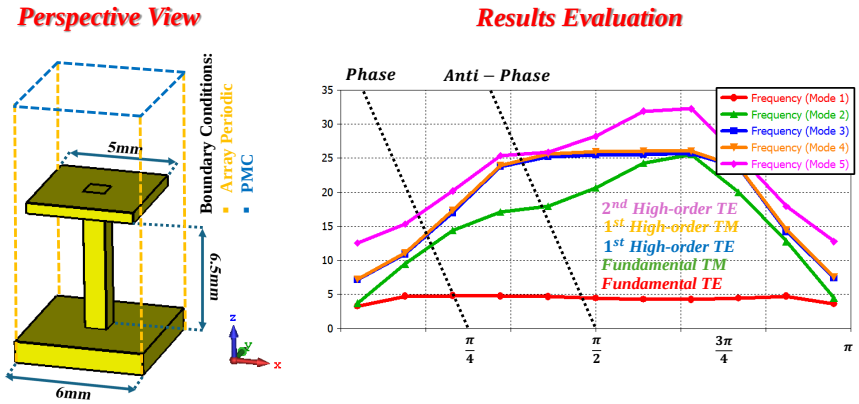



Figure 2.10: *Overview of the mushroom-like structure used in this study, accompanied of the dispersion diagram results for evaluation.*

in the referenced study. It is essential to note that while maintaining the concept of the source antenna, adjustments are made as necessary for impedance matching to accommodate the integration of metamaterials in this reactive near-field configuration. This approach ensures that both the antenna's performance and the metamaterial's effects are synergistically optimized for enhanced overall system performance.

We begin the study by scaling down the reference mushroom-like dispersion-engineered structure to the target frequency band and evaluating the dispersion diagram to determine if the higher-order modes could be appropriately positioned. It is important to inform that all the detail of such analysis are better explored in the next chapters of this thesis. In figure 2.10 it is explored the mushroom-like structure, demonstrating its dimensions and also demonstrating the wave modal behaviour expected when this is metasurface is introduced to the antenna concept. In the results, it can be how the modes behave over the variation of the frequency ($Y - axis$) versus the propagated wave phase($X - axis$). The phase and anti-phase lines are highlighted already taking into account the fringing fields expected due to coupling from one unit-cell of the metasurface to the neighbour, and outside of the array. Following the result curves, it can be noted that the phase line crosses the mode 1 (*Fundamental TE*) outside of our frequency band of interest, meaning that this mode will not resonate in our system. Differently, modes 2 (*Fundamental TM*), mode 3 (*First High-order TE*), mode 4 (*First High-order TM*) and mode 5(*Second High-order TE*), are crossed respectively at 13GHz, 14GHz, 14.1GHz and 16.5GHz, which are within our interest, demonstrating that they can effectively resonate in our system, if well excited by the source antenna. For the anti-phase line, it can be observed that mode 2 is being crossed at 17GHz, and the rest of the modes are at a higher frequency range, which is not covered here.

The subsequent step involves integrating the metasurface component with our source antenna and evaluating its behavior. For this purpose, an organized $4 \times 4$ array of mushroom-like structures was positioned above the source antenna, sharing the same ground plane. The optimized structure is depicted in Figure 2.11. Given the presence of multiple potential resonating modes within the antenna, attention is directed not only to the reflection coefficient but also to the real and imaginary impedance components. These plots are illustrated in Figure 2.12. Here, it is observable that the anticipated modes resonate within the frequency range of interest, with each exhibiting a notably

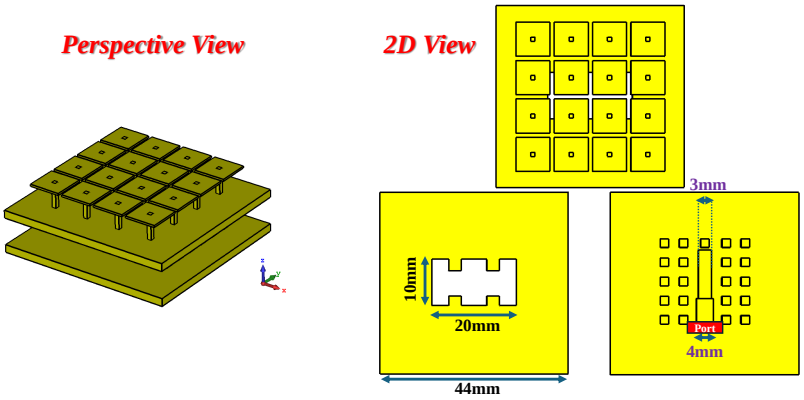



Figure 2.11: *Overview of the integration between the source antenna and the mushroom-like structure.*

high impedance characteristic typical of such components, often referred to as High Impedance Surfaces (HIS). Achieving impedance matching proves challenging due to these high impedance modes; however, partial matching within specific bandwidth segments is demonstrated for the purposes of this study. Notably, the anti-phase resonance around 17.3 GHz exhibits such high impedance behavior that it does not reflect in the reflection coefficient, as the matching network cannot adequately compensate for its impedance. Even for modes 1 and 5, which initially appear to have lower impedance, compensation in the feeding network remains inadequate, resulting in successful compensation only for modes 3, 4, and a portion of mode 5. Moreover, a hybridization effect between mode 2 and mode 3 is observed due to their close resonance frequencies, influencing the radiation pattern of the antenna despite the lack of matching in this specific frequency range.

To continue the analysis, we plot the radiation parameters at the resonance points for detailed examination. Figure 2.13 displays these parameters for observation. For modes 2 and 3, we observe significant hybridization, which causes the radiation pattern of mode 2 to exhibit side lobes around the main beam, deviating from its originally well-defined shape. Similarly, for mode 3, the side lobes become more pronounced than the boresight lobe, indicating that mode 3 is gradually dominating the radiation pattern. Mode 4's diagram, however, best represents what mode 3's pattern should ideally look like: reduced boresight radiation with stronger beams around $-35°$ and $30°$. This indicates that hybridization did not significantly affect mode 4. Mode 5's diagram clearly illustrates the transition from one high-order mode to another, showing a beam split into multiple radiation directions. Lastly, the diagram for mode 2's anti-phase resonance reveals a completely different radiation behavior, highlighting its unique characteristics.

In conclusion, the developed radiating component presented here, despite having no immediate practical application due to various parameter concerns and unconsidered factors, serves an educational purpose. This section of the thesis aims to explore the possibilities and demonstrate how such elements are created and evaluated, enhancing our understanding of metamaterial/metasurface integration with antenna concepts. It is also worth noting that the literature is rich with state-of-the-art concepts proposing various structures and designs for diverse telecommunications applications. Specif-

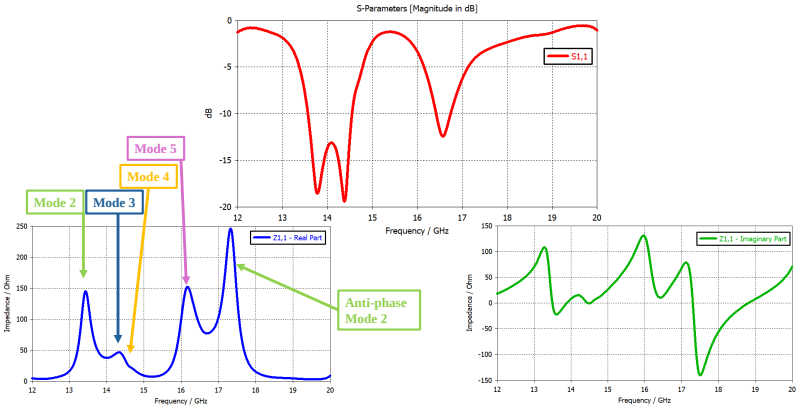



Figure 2.12: *Results for the reflection coefficient and the real and imaginary impedance parts for the integrated structure studied.*

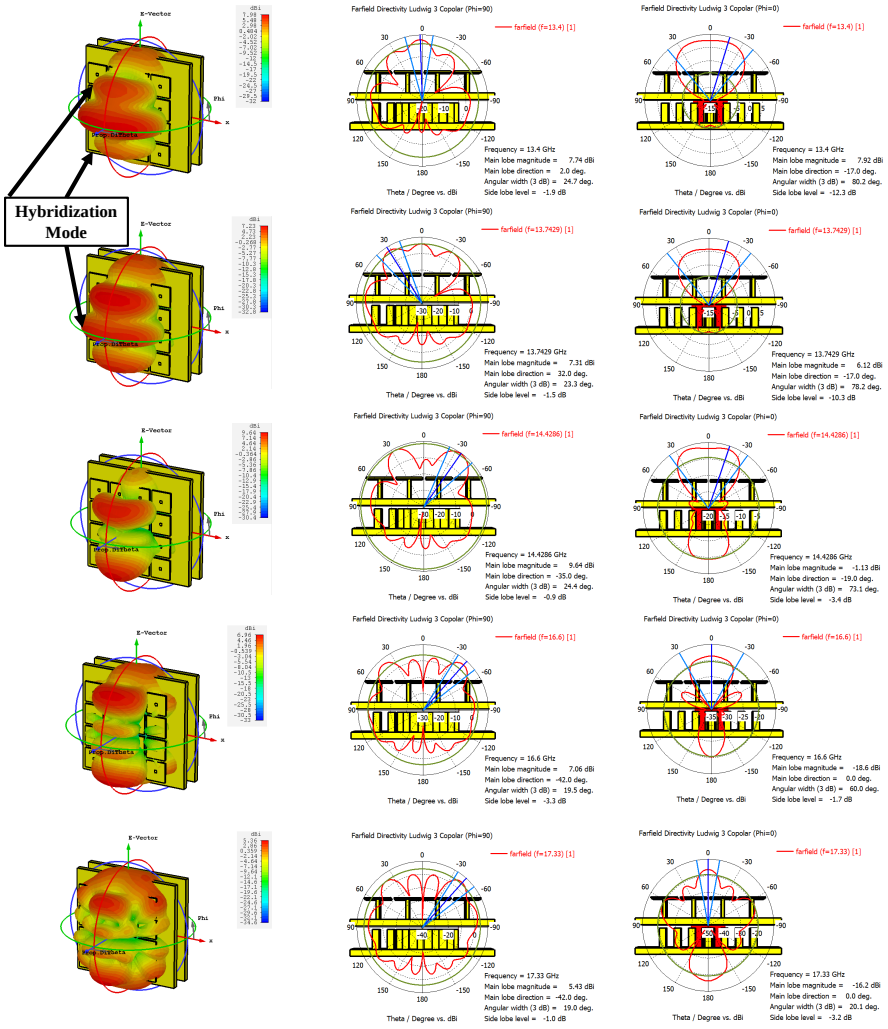



Figure 2.13: *Study of the radiation pattern for all modes accepted by the metasurface.*

ically, the term ”metaantennas” has gained traction, referring to antennas with integrated metasurfaces in their reactive near-field. This nomenclature reflects the growing interest and potential for expanding knowledge in antenna design.

## 2.4 Feeding System Application Example

As previously discussed, the manipulation of electromagnetic waves extends beyond radiating systems, encompassing passive feeding systems and components where field and current manipulation offer solutions for compactness and reduced losses. Metamaterials have been integrated into various passive components such as phase-shifters [16], power dividers, filters [17], and system routing [18], among others. Similar to the sections previously explained, the use of metamaterials and metasurfaces allows modifications to systems according to engineered design intentions, providing engineers with flexibility beyond traditional RF components. This section delves into the detailed application of gap waveguide (GW) technology, specifically the ridge gap waveguide, which leverages fundamental boundary conditions and the concepts of hard and soft surfaces to emulate a dispersion-engineered medium. This technology controls electromagnetic wave propagation within a parallel-plate waveguide [18]. The structured array used for demonstration purposes is akin to grounded metal pins [19], which can effectively emulate a dispersion-engineered solution similar to mushroom-like structures discussed earlier. The configuration of the system involves replacing the conventional ridged rectangular metal waveguide with a parallel-plate waveguide featuring unconnected conductors. One conductor consists of an array of pins, while the other remains unchanged. In a typical parallel-plate waveguide, solutions to Maxwell's equations are feasible due to perfect electric conductor boundary conditions on both metal plates, allowing independent electromagnetic wave propagation regardless of the plate spacing. Conversely, a metasurface-based waveguide modifies one of the conductors to achieve a perfect magnetic conductor boundary condition, which does not naturally occur in nature. By employing a dispersion-engineered array of pins, this condition can be emulated over a frequency bandwidth, effectively blocking electromagnetic wave propagation within the modified parallel-plate waveguide unless the spacing between plates is at least a quarter wavelength ($\lambda/4$). To emulate the ridged rectangular metal waveguide, a ridge can be inserted within the array of pins on the perfect magnetic conductor side of the parallel plate. This configuration traps an input signal within the confined ridged area, directing its path without leakage in undesired directions [18]. Similar to conventional waveguides, the permissible modes within this structure depend significantly on the dimensions of the removed pin area and the internal structure. Understanding the fundamental modes is crucial here, although higher-order modes can also be accommodated for feeding purposes, typical of any waveguide. For a comprehensive grasp of these concepts, it is advisable to consult current literature and state-of-the-art research, which continually refine and expand these technologies in telecommunications and RF engineering.

In Figure 2.14, we illustrate the structural differences when implementing a metasurface to create a ridge-gap-waveguide (RGWG). Electrically, both configurations function as waveguides with defined cut-off frequencies capable of guiding modes internally. However, the metasurface-based solution offers distinct advantages: it enables the creation of a more compact ridge waveguide and provides precise control over the cut-off frequencies of the guided modes by manipulating boundary conditions within the waveguide. This implementation method facilitates the design of miniaturized and cost-efficient systems, particularly advantageous for feeding closely spaced radiating

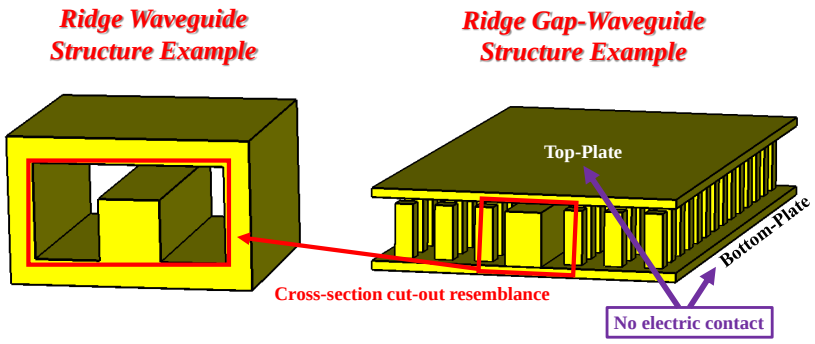



Figure 2.14: *Demonstration of the common ridge rectangular waveguide and the metasurface modified parallel-plate, named ridge-gap-waveguide.*

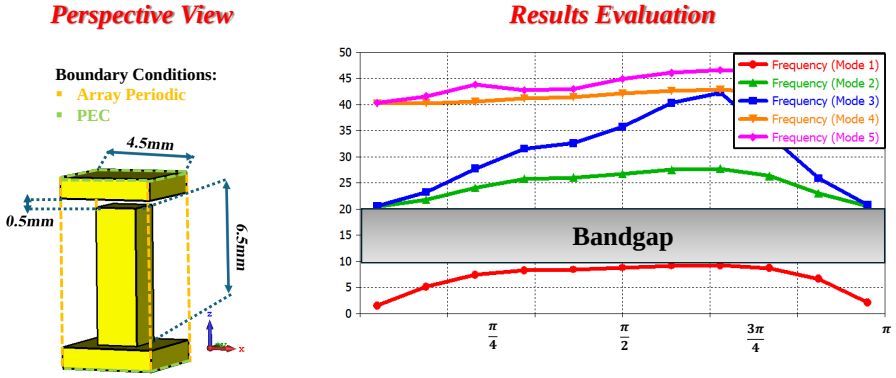



Figure 2.15: *Periodic pin geometry description and results of the modal allowance evaluation inside of the dispersion engineered structure.*

elements in antenna arrays, which would be challenging with traditional ridged rectangular waveguides. Moving to Figure 2.15, we present the simulated results obtained from the periodic pin configuration, which underscore the behavior of the structure based on dispersion diagrams. The top plate covers the structure without direct electrical contact, acting as the previously mentioned perfect electric conductor (PEC) surface. In contrast, the structure beneath each pin is directly connected, constituting the perfect magnetic conductor (PMC) surface. The separation between these surfaces dictates the cut-off frequencies of the modes within the waveguide, as depicted in the dispersion diagram on the right side of Figure 2.15. One notable feature highlighted in Figure 2.15 is the bandgap, an area where no modes exhibit resonance along the phase or anti-phase lines described in the previous section. This bandgap region represents a frequency range where wave propagation between the pins is forbidden, confining electromagnetic fields within specific areas such as the ridge region illustrated in Figure 2.14. This capability to create bandgaps is pivotal for applications requiring precise control over wave propagation and confinement, underscoring the versatility and utility of metasurface-based RGWGs in modern antenna and RF system designs.

If we revisit the source antenna studied in earlier sections of this thesis, we can now appreciate why its operational frequency band was chosen as 10 GHz to 20 GHz.

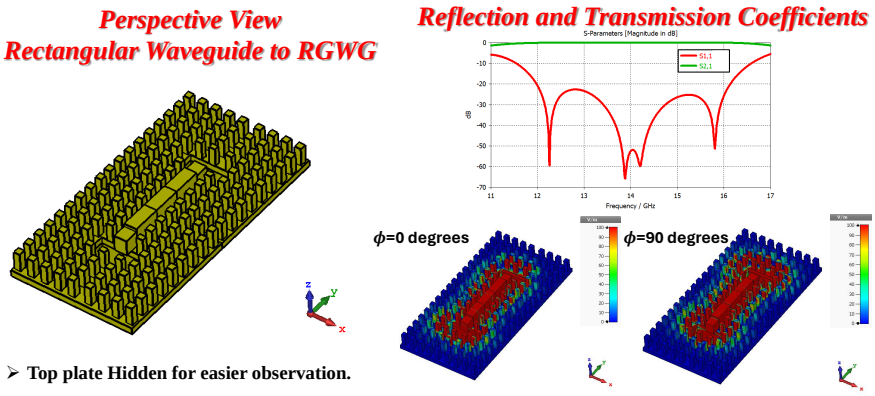



Figure 2.16: *Demonstration of the usage of the RGWG in a transition from a rectangular waveguide, highlighting the results and the E-field distribution.*

The reason lies in the feeding system's inherent bandwidth limitation caused by the bandgap region created within the dispersion-engineered structure. Specifically, the ridge inserted among the pins of the metasurface-based ridge-gap-waveguide (RGWG) confines quasi-TEM modes within the bandgap region, minimizing leakage and ensuring efficient wave propagation. Outside of this bandgap, different modes can propagate freely within the parallel-plate waveguide, altering the behavior of the metasurface PMC from its intended design. The practical application of this concept has been demonstrated in previous sections, particularly in its role as a feeding mechanism for both the source antenna and the metaantenna. In Figure 2.16, we present a simplified model and its surface electric field (E-field) distribution to illustrate how the fields are confined and behave within such a structure. In this model, we selected a straightforward rectangular waveguide (WG62) feeding arrangement, designed with an interface transition that efficiently converges the $TE_{10}$ mode into the quasi-TEM mode of the RGWG. This convergence facilitates effective energy transmission back to the waveguide, allowing analysis of transmission losses and bandwidth characteristics. Additionally, Figure 2.16 depicts the E-field distribution on the surface at 14 GHz, highlighting hot spots where the field is concentrated. The color scale, with blue indicating regions of minimal field intensity, visually illustrates the efficient field confinement achieved within the structure. This confinement is indicative of the performance observed in simulated results of reflection and transmission coefficients, demonstrating the efficacy of the dispersion-engineered RGWG in controlling electromagnetic wave propagation within specific frequency ranges.

In conclusion, the utilization of metasurfaces extends beyond traditional applications in radiating systems, encompassing advanced wave propagation manipulation. Metasurface-based waveguides represent a novel and disruptive approach to feeding mechanisms within RF technology, complementing and potentially surpassing existing solutions studied over the years. This underscores the transformative potential of metasurfaces in shaping the future frontiers of electromagnetics, paving the way for innovative advancements in antenna design and electromagnetic wave control.

# Chapter 3

# Chiral dielectric metasurfaces for broadband and highly integrable circularly polarized antenna

## 3.1 Introduction

THE quest for antennas that are cost-effective, compact, and efficient for a broad bandwidth with a specific radiation pattern relies on the ability to manage millimeter wave (mm-wave) electromagnetic field interactions. In order to transfer mm-wave antennas from research laboratories to the market of mobile infrastructures (i.e for 5G communication) and satellite communication, it is crucial to address polarization mismatches and suppress multipath interferences. In principle, this may be reached with circularly polarized (CP) antennas working at different ranges in the GHz regime [20–26], but two major limitations must be addressed. The first is to reach high-quality CP radiation with high gain within a broad bandwidth (BW). The quality of a CP electromagnetic wave is defined in terms of its axial-ratio (AR), i.e., the ratio between the major and minor axes of the polarization ellipse. The closer AR is to unity (0 dB) the higher the CP quality, and in practice electromagnetic fields have been considered as CP for AR below 3 dB [20–26]. As for the second drawback, one has to reduce the size and Ohmic losses (inherent in metallic inclusions) of mm-wave antennas to produce them in high-throughput, integrable platforms. Dielectric resonator antennas (DRAs) made with high-permittivity ($\varepsilon \sim 10 \cdots 10^2$) materials (e.g. ceramics) can concentrate and radiate CP electromagnetic fields with small losses [27]. However, the integration of these CP-DRAs into modern wireless systems is hampered by the need of multiple resonators and a multi-feed mechanism to achieve wide bandwidths [28–32]. Another possibility to address these limitations is to employ chiral systems in the design of CP antennas [33, 34]. Chirality refers to the handedness of an object which cannot be superimposed with its mirror image as in left- (LCP) and right-handed circularly polarized (RCP) light. The interaction of chiral electromagnetic fields with a chiral scatterer depends on this handedness. This may be used to simultaneously improve the handedness of an electromagnetic source while enhancing its electromagnetic field intensity, which can be reached through the proper engineering of suitable

chiral structures [35]. In fact, chirality concepts have been utilized to control electromagnetic wave propagation in the microwave and optical domains [36–38], which serves as inspiration for CP antenna design.

In this work, we demonstrate theoretically a new concept to produce integrated, highly efficient mm-wave CP antennas. In contrast to previous antenna designs using bulky metallic-based chiral metasurfaces [33,34], we exploit the pairing of electric and magnetic resonances of high-permittivity ($\varepsilon = 16$) cylindrical resonators with slanted slots at the center. An analogous concept in nanophotonics yielded an enhanced broadband near- and far-field chiroptical activity [38]. In order to reach optimized radiation patterns with high gain and wide AR-BW, we used a $2\times2$ arrangement of slotted cylinders. Through numerical calculations we show that this concept can be readily applied in antenna arrays by using a metal cavity surrounding each unit cell. The results for the system with metal cavity show promising improvements in gain and AR amplitudes and bandwidths. For comparison purposes, simulations were made using two commercial software packages for antenna design, namely CST Studio and ANSYS HFSS, and the results were in excellent agreement. CST Studio uses a time domain (transient) solver based on the finite integration technique (FIT) with a hexahedral mesh, whilst HFSS employs the finite element method (FEM) with tetrahedral mesh elements. As we shall demonstrate, antennas made with a chiral dielectric metasurface (CDM) are promising for tunable, broadband and efficient CP mm-wave radiation.

## 3.2 Antenna Design

### 3.2.1 Configuration

Figure 3.1 shows a zoomed view of the antenna designed to have the center frequency at 28.5 GHz to enable high-throughput applications in 5G and satellite communications. The antenna consists of five parts referred to as *i*) the bottom ground plane; *ii*) a substrate integrated waveguide (SIW) with a SIW-to-coax feeding; *iii*) a ground plane film; *iv*) a coax-fed driven patch antenna; and *v*) a chiral dielectric metasurface consisting of a $2 \times 2$ array of slotted dielectric cylinders. The ground plane films were considered as made of lossy copper. A top-view and side-view of the main building elements of the antenna design are presented in Figure 3.2. The SIW-based feeding layer is etched on a slab of Rogers RT/duroid 5880 ($\epsilon_r = 2.2$, $\tan\delta = 0.0009$) with thickness $h_{\mathrm{SIW}} = 0.5$ mm. A ground plane, $h_{\mathrm{sub}} = 0.035$ mm thick, was used to separate the SIW-feeding and the coax-fed driven-patch antenna. A CDM is stacked at the top of the structure, consisting of four slotted cylinders made of a ceramic dielectric material with $\epsilon_r = 16$, layered on a low-permittivity substrate of RT/duroid 5880 ($h_{\mathrm{meta}} = 0.5$ mm). The cylinders had a height $h_{\mathrm{cylinder}} = 0.8$ mm and diameter $d_{\mathrm{cylinder}} = 3.6$ mm, and were separated by a center-to-center distance of $dy_{\mathrm{c}} = 4.8$ mm. The slots at the center of the cylinders were parallelograms whose sides were labeled as $ls$ and $hs$ and the tilting angle is $\alpha$. The slots are rotated by an angle $\theta$ with respect to the $y$-axis, as depicted. CDM is fed by a driven patch localized below the low-permittivity layer at the center of the metasurface. The patch made of lossy copper had rectangular sides $sp$ and corner cuts $t_{\mathrm{size}}$. The coax-to-patch feeding line has a width $w_f = 0.8$ mm

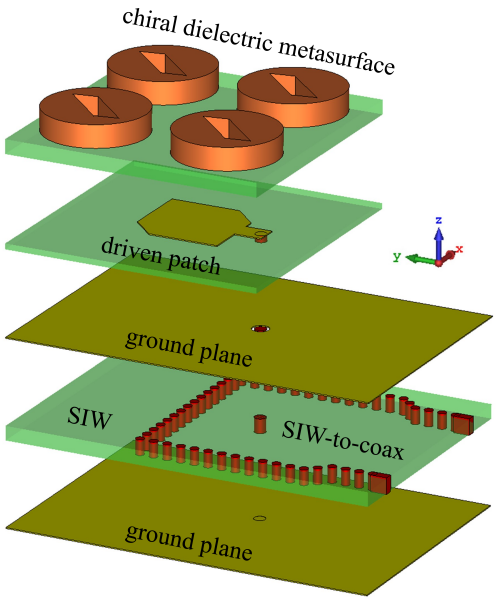



Figure 3.1: *3D geometric view of the proposed antenna element fed by a SIW ideal connector.*

and length $l_f = 0.85$ mm. The SIW-feeding structure is amenable to integration with planar front-end circuits. The SIW structure was designed as a rectangular waveguide input, forming a SIW-to-coax transition where the distance between the pin and the shorting wall was tuned for impedance matching [39, 40]. The dimensions of the SIW-feeding and the remaining parameters are listed in the caption of Figure 3.2. It is worth mentioning that with the antenna size taken as $0.95\lambda_0 \times 0.95\lambda_0$ ($\lambda_0$ at the center frequency of 28.5 GHz), our concept enables the application of high directive antenna array systems by designing the structure to be directly fed by a coax-wire.

### 3.2.2 Working principle and enhancement of ARBW

Dielectric resonators with high-permittivity are known to support electric and magnetic resonances of different orders [27,29], in analogy with cylindrical nanostructures [38]. The near-field overlapping between nearby cylinders resembles the electronic-bands from well-localized atomic orbitals in the tight-binding model [41, 42] in electromagnetic platforms known as metasurfaces. Here, we use dielectric cylinders with a slanted slot at the center to produce integrable, highly efficient and broad ARBW CP antennas. An analogous concept was exploited in nanophotonic platforms to produce giant enhancement of chiroptical effects [38]. The concept is based on the coupling of the electric and magnetic modes of the resonators (considered as dipoles in a qualitative approximation) which can be expressed as

$$\tilde{\mathbf{p}} = \tilde{\alpha}\tilde{\mathbf{E}} - i\tilde{G}\tilde{\mathbf{B}}, \qquad \tilde{\mathbf{m}} = \tilde{\chi}\tilde{\mathbf{B}} + i\tilde{G}\tilde{\mathbf{E}}, \tag{3.1}$$

where $\tilde{\mathbf{p}}$ and $\tilde{\mathbf{m}}$ are the electric and magnetic dipoles, respectively. $\tilde{\alpha}$ and $\tilde{\chi}$ are the complex electric polarizability and magnetic susceptibility, whilst $\tilde{G}$ corresponds to the mixed electric-magnetic dipole polarizability. $\tilde{\mathbf{E}}$ and $\tilde{\mathbf{B}}$ are the complex electric and magnetic fields. The radiated electromagnetic energy has, therefore, a term $\sim$

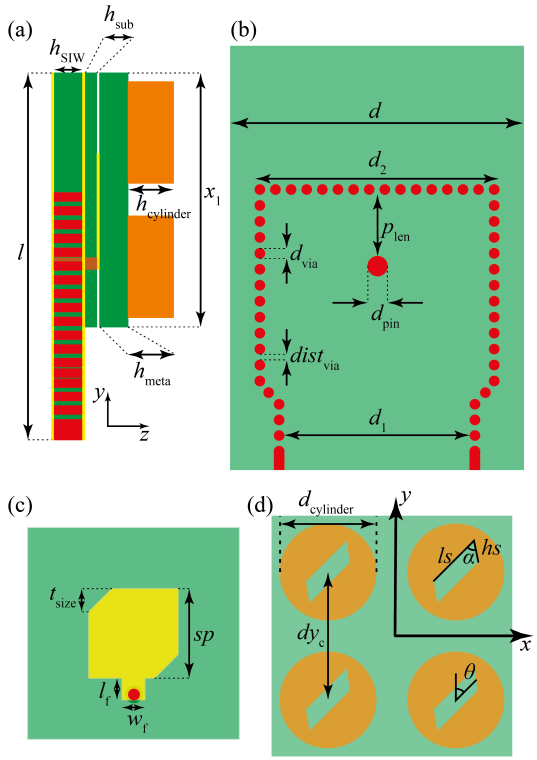



Figure 3.2: *(a) Parametric side view of the antenna layers divided as: (b) SIW-to-coax feeding, (c) driven patch layer and (d) chiral dielectric metasurface layer. The design parameters are* $x_1 = 10$ *mm,* $d = 10$ *mm,* $d_2 = 7.5$ *mm,* $p_{\text{len}} = 2.15$ *mm,* $d_{\text{via}} = 0.3$ *mm,* $d_{\text{pin}} = 0.4$ *mm,* $dist_{\text{via}} = 0.19$ *mm,* $d_1 = 5.71$ *mm,* $t_{\text{size}} = 0.86$ *mm,* $sp = 3.3$ *mm,* $l_f = 0.85$ *mm,* $w_f = 0.8$ *mm,* $ls = 2.1$ *mm,* $hs = 0.8$ *mm,* $\alpha = 60°$ *and* $\theta = 45°$.

$\tilde{G}''\text{Im}\left\{\tilde{\mathbf{E}} \cdot \tilde{\mathbf{B}}\right\}$, where $\tilde{G}''$ stands for the imaginary part of $\tilde{G}$. It is just at the slanted sides $hs$ where $\tilde{\mathbf{E}}$ and $\tilde{\mathbf{B}}$ become mixed [38], allowing the tuning of $\tilde{G}$ through the tilting angle $\alpha$ (see Figure 3.2(d)). The electromagnetic fields exciting the CDM are produced by a single narrow-band driven-patch antenna with truncated corners, thus being constantly fed by two orthogonal linearly polarized modes ($\text{AR} \gtrsim 5$) (see Figure 3.3).

## 3.3 Results and discussion

The individual contributions from the building components in the antenna design can be studied by analyzing the results in Figure 3.3 for $S_{11}$, AR and boresight gain for the patch without (W/O) metasurface (dashed lines) and with the metasurface of solid cylinders (solid lines) depicted in the inset of Figure 3.3(a). Calculations in this figure were made using the commercial software CST Studio. Results for $S_{11}$ are presented in Figure 3.3(a), whereas the corresponding AR and boresight-gain are shown in Figure 3.3(b). Poor values for the impedance-matching ($S_{11} \gtrsim -10$) and gain ($< 8$) are observed for the patch W/O metasurface. The antenna with the metasurface containing the solid cylinders improves the impedance-matching, AR values and boresight gains, in addition to an improved bandwidth performance. Such improvements are due

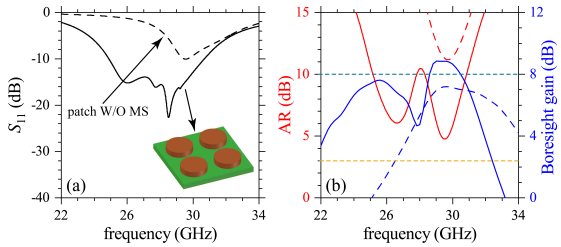



Figure 3.3: *Numerical results for (a) $S_{11}$ and (b) AR and boresight gain. Solid and dashed lines are for the patch antenna with and without (W/O) the DR metasurface. Simulations were carried out using the commercial software CST Studio. Horizontal dashed lines in (b) are eye guides for $AR = 3$ dB and boresight gain=8 dB.*

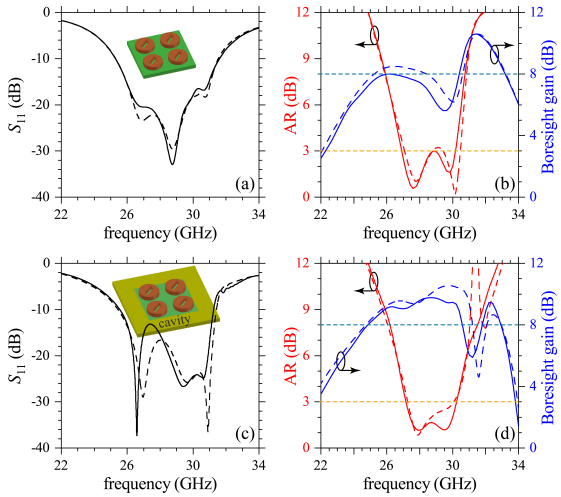



Figure 3.4: *Numerical results for $S_{11}$, AR and boresight gain are presented for the CDM-based antenna (a)-(b) with and (c)-(d) without the metal cavity. Simulations from CST Studio and ANSYS HFSS are indicated by solid and dashed lines. Horizontal dashed lines in (b) and (d) are eye guides for $AR = 3$ dB and boresight gain=8 dB.*

to the dielectric cylindrical resonators and their corresponding near-field interactions. However, the radiation and AR performances are still low in all of these results, and additional strategies are required to design useful CP antennas.

Following the reasoning of chiral dielectric metasurfaces for enhanced chiroptical effects [38], we considered slanted slots etched at the center of each cylinder, as schematized in the inset of Figure 3.4(a). This mechanism not only improved AR but also the whole operating performance of the antenna, as it can be seen from Figures 3.4(a) and 3.4(b). Calculations from CST Studio and ANSYS HFSS are presented with solid and dashed lines, respectively. Negligible differences are observed due to different convergences of the software packages. The applicability of this CDM-based CP antenna is demonstrated in Figures 3.4(c) and 3.4(d) with AR and gain corresponding to the system surrounded by a metal cavity (considered as made of Al). This cavity surrounding the four-element CDM enables integration into antenna arrays by suppressing the mutual coupling between adjacent elementary cells. Although a small decrease was induced by the cavity in the impedance $\mathrm{BW} = [25.5\ \mathrm{GHz}, 31.3\ \mathrm{GHz}]$ and 3-dB $\mathrm{ARBW} = [27.1\ \mathrm{GHz}, 30.3\ \mathrm{GHz}]$, in relation to the impedance $\mathrm{BW} = [25.3\ \mathrm{GHz}, 31.6\ \mathrm{GHz}]$ and 3-dB $\mathrm{ARBW} = [26.9\ \mathrm{GHz}, 30.2\ \mathrm{GHz}]$ for the system with-

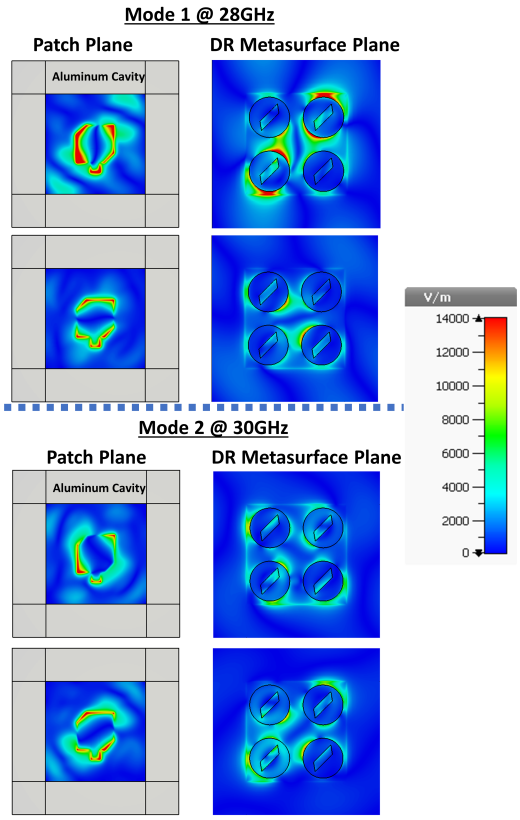



Figure 3.5: *Simulated* ***E****-field of the antenna element at orthogonal phases for both CP modes and both planes: Patch and DR Metasurface Planes.*

out cavity, the corresponding gain ($\gtrsim 9$) and AR ($\mathrm{AR} \ll 3$) were considerably improved. Moreover, a gain notch from Figure 3.4(b) was shifted out of the bandwidth range of interest when using the cavity, which certainly improves the CP radiation performance. Figure 3.5 shows the **E**-field distribution for the two orthogonal modes of the patch coupled to the CDM. These fields were calculated for the frequencies at which AR achieves the best results, see Figure 3.4(d). For illustrative purposes, results are presented for **E**-field distribution at the patch and CDM planes, and with radiation of an LCP electromagnetic field. As it can be inferred, an RCP antenna can be developed using the mirror image of CDM and the patch antenna. The evanescent behavior of the electromagnetic field in the cavity is also evidenced.

The numerical results from hereon were obtained with the commercial software CST Studio for the antenna without the cavity. Results of the LCP (co-polarized) and RCP (cross-polarized) radiation patterns for the CDM-based antenna are presented for 27.5 GHz and 30 GHz in Figures 3.6(a)-(b) and 3.6(c)-(d), respectively. For the co-polarized radiation at the $\phi = 90°$-plane, a 3-dB power beamwidth of $66.3°$ (in the range from $38.3°$ to $-28°$) is observed for 27.5 GHz (Figure 3.6(a)) while for 30 GHz it is $58.7°$ (from $31°$ to $-27.7°$) (Figure 3.6(c)). The condition $\mathrm{AR} \leq 3$-dB is met when the difference between the co-polarized and cross-polarized patterns is $\geq 15$-dB. Therefore, there is a high AR performance in the whole 3-dB power beamwidth for the 27.5 GHz mode, but not for 30 GHz which is limited to $43°$ (from $23°$ to $-20°$). In the

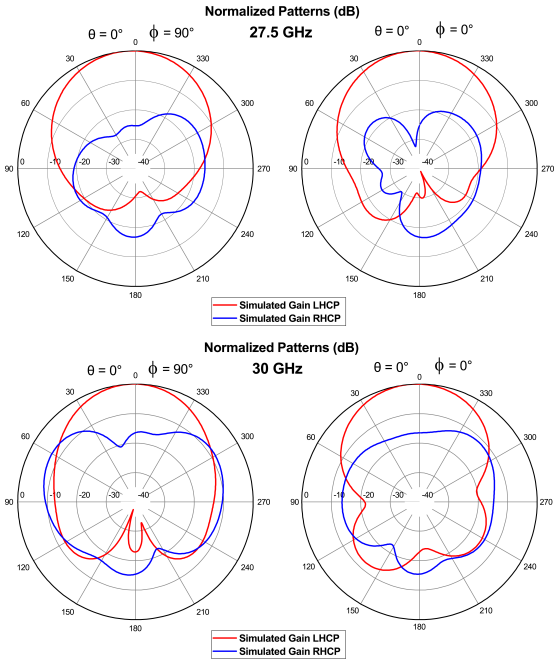



Figure 3.6: *Simulated radiation patterns at 27.5 GHz and 30 GHz for both cut-planes.*

case of $\phi = 0°$-plane, there is nearly the same 3-dB power beamwidth for both modes, $66.3°$ (in the range from $36.3°$ to $-30°$) for 27.5 GHz and $62.7°$ (in the range from $36°$ to $-26.7°$) for 30 GHz. However, the 3-dB AR performance for 30 GHz exhibits a very narrow beamwidth of $36°$ (from $24°$ to $-12°$), in contrast to 27.5 GHz that stays with at least 15-dB difference between the co-polarized and cross-polarized radiation patterns in the whole 3-dB power beamwidth. Hence, the area covered by the 27.5 GHz mode is larger than for the 30 GHz.

## 3.4 Parametric Study

In order to understand how different design parameters affect the functioning of the meta-antenna, we plotted $S_{11}$ and AR for different values of $\theta$, $d_{\text{cylinder}}$, $l$s and $dy_{\text{c}}$ in Figures 3.7 and Figure 3.8. There is a slight narrowing of the impedance bandwidth for increasing $\theta$ in Figure 3.7(a), in contrast with the loss of CP radiation ($\text{AR} > 3$) in Figure 3.8(a). This dependence of AR on $\theta$ highlights the importance of this parameter when designing the metasurface to obtain high-performance CP radiation. Upon increasing $d_{\text{cylinder}}$ the modes in $S_{11}$ are discretized with loss in the ability to generate CP radiation as indicated by the poor AR values ($\text{AR} > 3$) in Figure 3.8(b). The latter behavior is explained by recalling that the CDM modes should be matched with the two orthogonal modes from the driven patch for a proper coupling and field re-radiation. Another important parameter in the design is the length $ls$ of the slots, which can be varied to tune AR (and its bandwidth) to its optimum values with small changes of $S_{11}$, as noted in Figure 3.7(c) and 3.8(c). The interaction of nearby cylinders in CDM depends on $dy_{\text{c}}$ which then affects the quality of CP radiation. Figures 3.7(d) and 3.8(d) point to a decrease in the ability to produce CP mm-waves upon increasing $dy_{\text{c}}$. Excitation of several out-of-phase resonances occurs for very small $dy_{\text{c}}$ which,

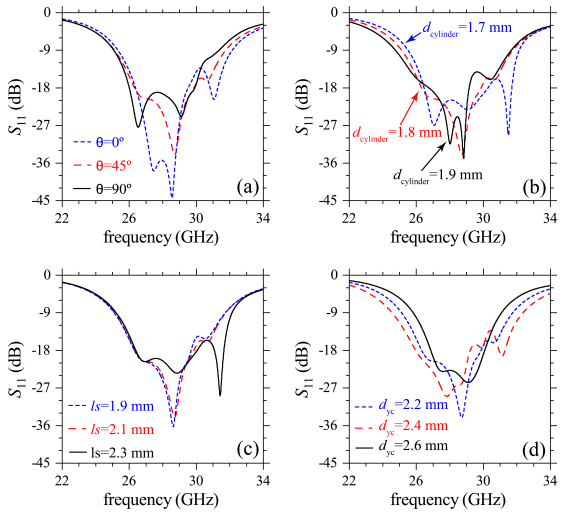



Figure 3.7: *Simulated parametric study for reflection coefficient of the proposed antenna. (a) variation of $\theta$, (b) variation of $d_{cylinder}$, (c) variation of $ls$ and (d) variation of $dy_c$.*

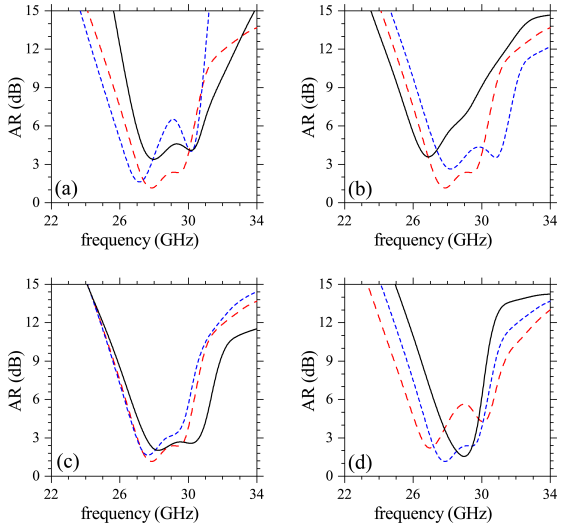



Figure 3.8: *Simulated parametric study for AR of the proposed antenna. The variation of (a) $\theta$, (b) $d_{cylinder}$, (c) $ls$ and (d) $dy_c$ was the same as in Figures 3.7(a)-(d), respectively.*

despite widening the impedance bandwidth, negatively affect AR.

The competitiveness of our CDM-based antenna is demonstrated by comparing with recent proposals for CP antennas in Table 5.1, where results are given for the central frequency, impedance bandwidth (BW), ARBW, 2-dB gain bandwidth, and peak gain. We avoid comparing sizes because of the nature of the antenna and the corresponding operating frequencies. However, we emphasize that the CDM in this work has a reduced size while maintaining its efficiency. Moreover, there is a high peak gain with low gain variation in a wide bandwidth which is broader than in reports in the literature. Therefore, we expect that this work will stimulate the use of CDMs to produce CP radiation in other antenna designs.

Table 3.1: *Performance Comparison among CP Antennas*

| Designs | Freq. (GHz) | BW (%) | 3dB-ARBW (%) | 2dB-Gain-BW (%) | Peak Gain (dBic) |
|---|---|---|---|---|---|
| Ref. [24] | 3.5 | 21 | 8.5 | 19 | 6.5 |
| Ref. [26] | 26 | 12.5 | 26 | 18 | 7.5 |
| Ref. [30] | 5.5 | 25.4 | 22.8 | 34.2 | 7.7 |
| Ref. [31] | 11.7 | 27.8 | 24 | 16.5 | 10 |
| this work* | 28.5 | 22.6 | 11.6 | 34 | 8.5 |
| this work** | 28.5 | 20.4 | 11.2 | 19.4 | 10.4 |

* - W/O cavity, ** - with cavity

## 3.5 Chapter Conclusions

The introduction of a chiral metasurface on the design of low-profile CP DRAs has been shown to yield a wide AR bandwidth, high-gain and low AR values. Of special relevance is the compactness of the CP antenna designed, suitable for mobile communication systems. The concepts and design were validated through numerical simulations using two commercial software packages, and no significant difference was noted in the results obtained with CST Studio and ANSYS HFSS. From these simulations one learns that the CP antennas can be tunable and integrated into front-end circuits or phase-arrayed systems (directly fed by a coax-wire). The design also included materials and conditions which are readily available for implementation, and therefore we may expect the fabrication of CP antennas for high throughput 5G and satellite communications in the $Ka$-band.

# Chapter 4

# Integrated Wideband Dual-Polarized ME-Dipole Planar Antenna Array with Tight Coupled Elements

## 4.1 Introduction

The exploitation of mmWave frequencies has triggered great research interest to cope with the ever increasing demand for higher data rates and greater capacity in wireless communication networks [43, 44]. In particular, high-performance mmWave antennas are key components for the implementation of future fifth-generation (5G) wireless communication systems [45–48], with current developments including automotive radars [49], satellite communications [50] and wireless point-to-point communications [51]. Despite these advances, approaches are mostly based on the use of all-metal building elements (which are bulky and heavy) and printed circuit board (PCB) antennas, which are hampered by the high level of Ohmic and dielectric losses at mmWave frequencies [50–52]. On the other hand, high-performance dual-polarization wideband radiators (covering a vast range of frequencies), with stable radiation patterns, are required to improve data link capacities and reduce multipath fading [47].

Attempts to overcome these drawbacks include the use of gap-waveguide technology for feeding networks which, in contrast to substrate integrated waveguides (SIWs) and microstrip fed antennas, offers lower losses, easy fabrication and compactness at mmWave regime. Moreover, straightforwardly manufacturable magneto-electric (ME) dipole antennas have demonstrated stable dual-polarization radiation performances within wide bandwidths, offering easy integration with mmWave front-end circuits [46, 47, 53–55]. Indeed, recent wideband dual-polarized ME-dipole antennas have demonstrated the ability to produce wide impedance bandwidth with unidirectional radiation patterns within the entire working frequency range. Nevertheless, conventionally used $\Gamma$-shape probes (to feed the radiators) need complex multilayer (with different plated vias implementation) and tuning techniques for wideband impedance matching.

In this work, we combine the concepts of ME-dipole and tightly-coupled array elements (fed by an integrated gap-waveguide) to design a new radiating concept of

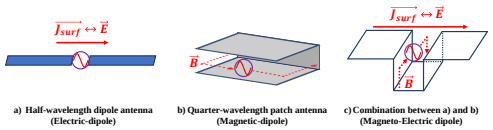



Figure 4.1: *Principle of generating the ME-dipole response from a structure perspective. Adapted from [2]*

high-performance integrated dual-polarized mmWave antenna. Remarkably, our idea reduced the whole size of the antenna array element through the use of a shared aperture. Moreover, the use of a cavity backed slot etched in the ground plane, in contrast to conventional Γ-shape probes, reduces the complexity of the design and enables a way for future highly integrable devices. Finally, air cavities and gap-waveguides were integrated in the antenna design to reduce the overall dielectric and transmission losses, respectively.

## 4.2 The ME-Dipole Concept

The term ”Magneto-Electric dipole” was first introduced in 2006 by Luk and Wong [56], marking a significant innovation in the field of complementary antennas. They achieved a wideband and stable antenna element by integrating complementary antenna concepts into a single structure. The fundamental design consists of a planar electric dipole combined with a vertically shorted quarter-wave patch antenna, as schematically shown in Figure 4.1, which provides a generalized illustration of this concept. Typically, the antenna is excited using a proximity-coupled feed, allowing it to operate as a combination of electric and magnetic dipoles [57]. This design offers a broad impedance bandwidth, stable gain, and consistent radiation patterns, with low levels of cross-polarization and back radiation across its entire operating frequency range. Subsequent research has explored the development of Magneto-Electric dipoles with various polarizations for different applications, such as ultra-wideband (UWB) and 60 GHz wireless communications, and the introduction of other types of complementary antennas [2, 57, 58].

A linearly polarized complementary antenna features orthogonal electric and magnetic dipoles, which can be positioned together or slightly apart. The radiation pattern of an electric dipole resembles a figure-8 in the E-plane and a figure-O in the H-plane, whereas a magnetic dipole exhibits the opposite pattern. When these dipoles are co-located and excited with equal power and phase, the resulting radiation pattern forms a cardioid shape, providing identical patterns in both the E-plane and H-plane. This configuration significantly reduces back radiation, which is advantageous for communication systems. This effect is demonstrated in Figure 4.2.

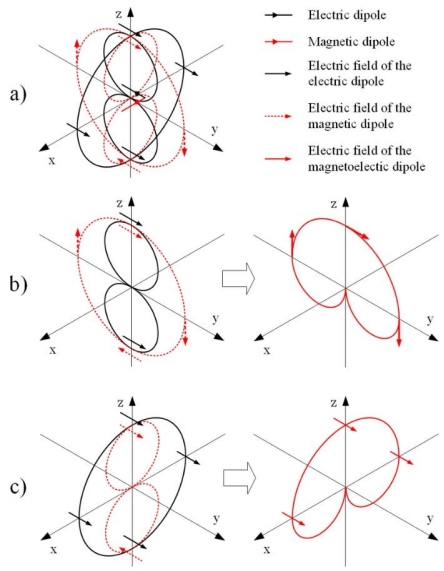



Figure 4.2: *Demonstration of the ME-dipole background conceptualization. Adapted from [3]*

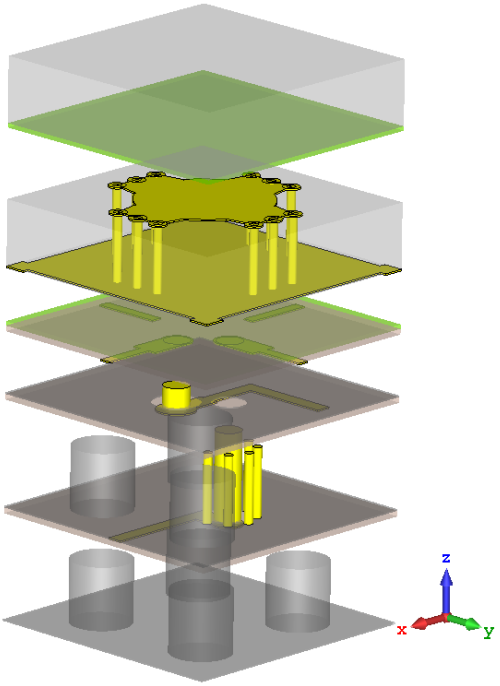



Figure 4.3: *Schematic representation of the proposed antenna design.*

## 4.3 Antenna Structure

### 4.3.1 Element Design

Figures 4.3 and 4.4 show a schematic representation and a side-view of the building layers of the antenna design, respectively. The complete radiating element consists of five parts, which from top to bottom are referred as *i*) superstrate; *ii*) modified bowtie radiator; *iii*) air-filled cavity backed layer; *iv*) vertical polarization feeding layer; and *v*) horizontal polarization feeding layer. It should be noted that both linear polarizations

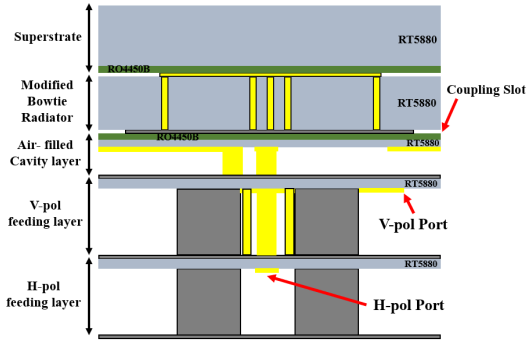



Figure 4.4: *Side-view of the antenna shown in Fig. 4.3, used to point out the feeding layers and other building elements.*

can be excited through different ports, with different feeding layers. We used a cavity backed coupling slot and a modified bowtie patch to simultaneously excite the electric and magnetic resonances of a ME-dipole antenna, thus exhibiting broad bandwidth and stable unidirectional radiation patterns. In particular, each slot is fed by a perpendicular probe localized at the cavity layer, as illustrated. The power is transferred to the probes by two different layers, one for the vertical polarization (V-pol) and the other for the horizontal polarization (H-pol), localized below the air-cavity. Then, a periodic bed of pins (behaving as a high-impedance surface) is used to create a stop band along the interest bandwidth in a modified microstrip gap waveguide. Indeed, since the distance between the opposite flat surfaces inside the cavity is less than a quarter-wavelength, propagation will only occur when the microstrip is inserted.

Simulations for the unit cell were carried out using periodic boundary conditions (PBCs). Therefore, the coupling slots and probes are in sequence along both $x$- and $y$-coordinates depicted in Fig. 4.3. The unit cell size is $6 \times 6 \times 7$ mm$^3$. The material for the substrates in the feeding layers and below the bowtie, as well as for the superstrate, was chosen as Rogers RT5880 ($\epsilon_r = 2.2$ and $\tan\delta = 0.0009$), whilst for the bonding layers between the superstrate and bowtie patch, and also between the cavity layer and the bowtie's reference ground plane we used Rogers RO4450B ($\epsilon_r = 3.7$ and $\tan\delta = 0.004$), as indicated in Fig. 4.4.

### 4.3.2 Radiator Operating Mechanism

To solidify the understanding of the proposed concept, we explain the operating principle of the previously demonstrated radiator unit cell. Figure 4.5 provides a step-by-step evolution, illustrating how a single polarized dipole over a ground plane can be extended to form a single polarized shared aperture array, and subsequently evolve into a dual polarized shared aperture tightly coupled array.

Although this configuration resembles a patch radiator when the dipoles are combined, an analysis of the current distribution reveals that the dipole mode remains dominant over the aperture mode. This dominance enables the formation of a tightly coupled dipole array within the shared aperture. Notably, within the patch elements, a current null always occurs at the center. This null is a result of opposite current phases meeting as they flow toward the patch center, indicating that each patch does not func-

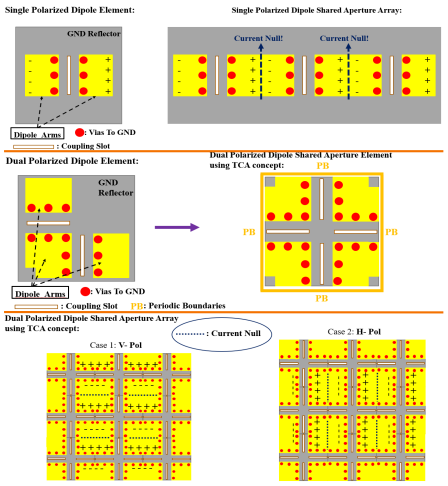



Figure 4.5: *Radiation mechanism description from the shared aperture concept.*

tion as a single antenna element. Instead, it is the combination of a single slot feeding into the two sides of the dipole arms surrounding it.

### 4.3.3 Dual Layer Feeding Mechanism

Since the energy propagating path (up to the cavity layer) for the bottom feeding layer is longer than for the upper feeding layer, we should consider both feeding layer designs separately. First, for the upper layer we used a via transition through the ground plane, which reached the V-pol feed probe localized in the air filled cavity. Second, for the bottom layer we used an emulated coax, like the one proposed in [59], to have a stable wideband impedance transition from the bottom to the H-pol feed probe in the air cavity.

Due to the wideband feature of the radiating element, we used a modified gap-waveguide technology [60] to achieve wide-stop bands, supporting the development of wideband power dividers for planar array implementation.

### 4.3.4 $4 \times 4$ Planar Array

As described before, one of the challenges for wideband tight coupled arrays is the development of power dividers enabling stable performance, with no phase difference applied to each element in the array. More specifically, the challenge consists in designing a structure capable of, when integrated with the fed elements, produce reflection coefficients low enough and less than -10dB along the entire impedance bandwidth. These requirements are met in this work by tapered transitions for the power dividers (producing smooth impedance transitions), achieving reflection coefficients lower than -22 dB for the $4 \times 4$ feeding over the entire band of interest. The corresponding feeding layer designs for V-pol and H-pol are shown in Figures 4.6a) and 4.6b), respectively.

The proposed $4 \times 4$ array antenna design is presented in Fig. 4.7. A grounded

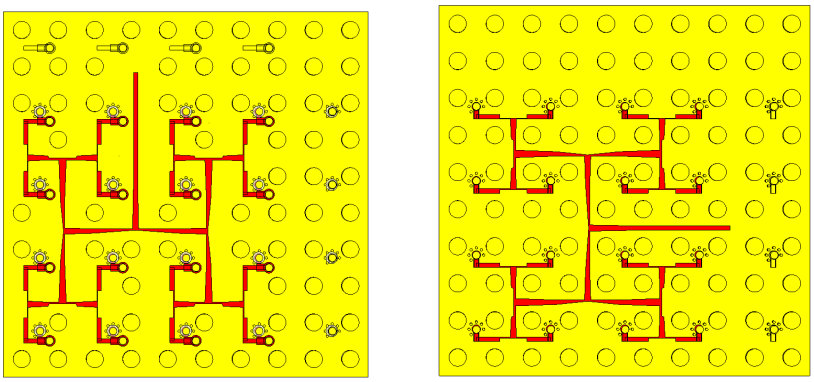


Figure 4.6: *V-pol and H-pol feeding networks using the modified inverted microstrip gap waveguide.*

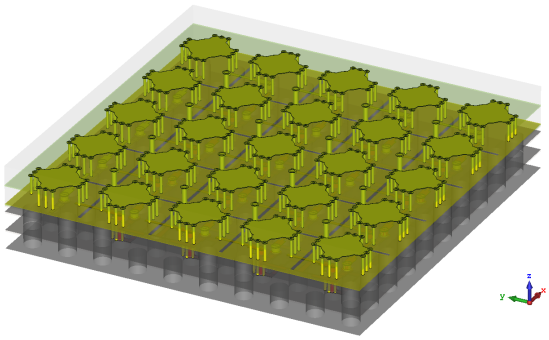


Figure 4.7: *Pictorial representation of the* $4 \times 4$ *planar array antenna design.*

via is placed between the upper slots to avoid detrimental effects on the radiation pattern, induced by the electromagnetic surface waves in the bowtie's plane. Since the via supports better elements isolation when integrated to the planar antenna configuration, improved radiation patterns (without altering other antenna features) are obtained. After integrating this last element, the final size of the device was $30 \times 30 \times 7$ mm$^3$.

## 4.4 Simulation

Results in this work were obtained using full-wave simulations through the commercial software CST Microwave Studio. Numerical data for the $|S_{11}|$, $|S_{12}|$, and $|S_{22}|$ parameters are shown in Fig. 4.8. $|S_{11}|$ and $|S_{22}|$ represent the reflection coefficients for V-pol and H-pol input ports, respectively, whereas $|S_{12}|$ corresponds to the mutual coupling between these signals. The bandwidth for the coaxial emulated H-pol port, 73.3% (15.2 GHz-32.8 GHz), is wider than for the V-pol port, 68.6% (16.1 GHz-32.9 GHz), due to the controlled and stable wideband impedance transition. Importantly, future optimizations of the proposed device may allow for better and stable full-array behavior solutions. In relation to mutual coupling, we note that $|S_{12}|$ remains below -20 dB along the entire operation bandwidth. In fact, except for the peak close to 25 GHz (associated to a weak common mode resonance), due to the proximity between both probes inside the air cavity, the $|S_{12}|$ values are found below -22 dB.

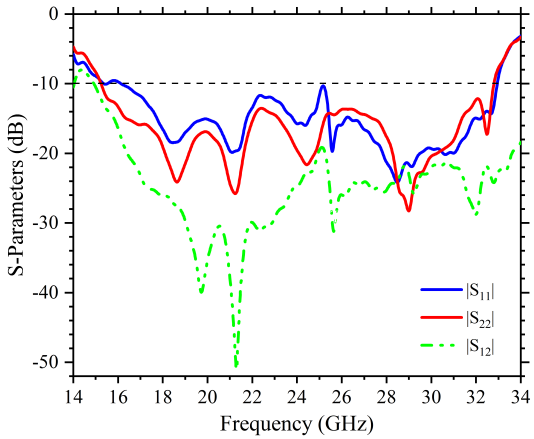



Figure 4.8: *$|S|$-parameters for the $4 \times 4$ planar antenna array. $|S_{11}|$ and $|S_{22}|$ are the reflection coefficients for V-pol and H-pol input ports, respectively, and $|S_{12}|$ represents the coupling between the V-pol and H-pol ports.*

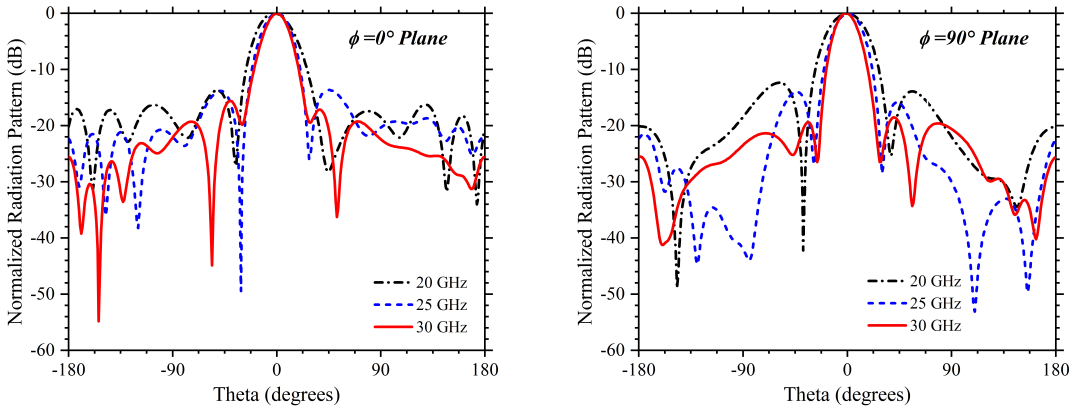



Figure 4.9: *Radiation patterns for both cut planes when fed by the V-pol input port.*

The normalized radiation patterns at 20 GHz, 25 GHz and 30 GHz are shown for V-pol and H-pol in Figures 4.9 and 4.10, respectively. From these results we observe almost the same response when rotating the cut planes, i.e., the radiation pattern for V-pol at the $\phi = 0$ plane is closely equal to the H-pol at the $\phi = 90$ cut plane, which is due to the dual polarization scheme of the antenna design. Each radiation pattern was normalized to its maximum amplitude. The simulated gain varied from 11 dBi to 18.5dBi. More specifically, we obtained 14.3 dBi, 16.1 dBi and 18.1dBi for 20 GHz, 25 GHz and 30 GHz, respectively, with small variations between both H-pol and V-pol polarizations. Significantly, through the tight-coupled elements implementation, a side-lobe level of at least -12.6 dB was reached for the entire bandwidth.

## 4.5 Chapter Conclusions

A wideband dual-polarized ME-dipole planar array, using the concepts of tight-coupled elements, fed by a modified gap-waveguide is presented in this paper. The feasibility of our proposal was confirmed by simulations of a $4\times4$ planar array antenna.

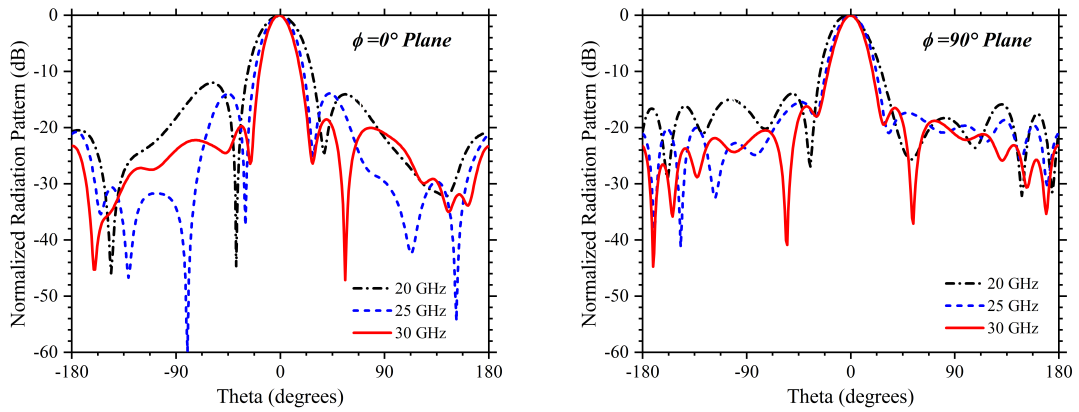



Figure 4.10: *Radiation patterns for both cut planes when fed by the H-pol input port.*

The impedance bandwidth for vertical and horizontal polarizations achieved 68.6% and 73.3%, respectively, with a maximum gain of 18.5 dBi. Since the all materials and geometries considered in this work can be easily implemented by low-cost PCB fabrication methods, we hope our idea stir significant interest for the design and development of future high-performance integrated dual-polarized antennas for mmWave applications. To the best of the authors' knowledge, the proposed antenna has the widest bandwidth for either dual-polarized ME-dipole planar arrays and antenna arrays based on gap waveguide technology. Besides, our concept can be straightforwardly extended to larger arrays without the need of additional layers.

# Chapter 5

# All-Metallic-Metasurface-Based Wideband Dual Fabry-Perot Resonance Antenna Array with High Directivity and Polarization Purity

## 5.1 Introduction

Owing to their exceptional and unequal electromagnetic features, metamaterials and metasurfaces are currently being leveraged to overcome limitations in antenna design. Unlike conventional approaches rooted in decades-old antenna theory, which often grapple with issues such as bandwidth, gain, radiation pattern behavior, and efficiency, the synergistic combination of metasurface concepts with antenna theory is pushing the boundaries of modern antenna engineering [7, 8, 61]. Indeed, recent advancements have demonstrated the potential of modern antennas to achieve directivity, bandwidth, radiation pattern, polarization, and beam shaping previously thought unattainable, thanks to the integration of metasurface technologies [62–65]. A metasurface is an artificial material comprised of two-dimensional arrangements of scatterers with dimensions smaller than the operating wavelength, known as sub-wavelength elements. This characteristic design facilitates meticulous manipulation of electromagnetic fields tailored to precise requirements, providing unparalleled control and versatility in antenna design [7, 66]. Recent applications showcasing the versatility of this approach include the design of transmit-reflect arrays, where metasurfaces are utilized to create surfaces that exhibit lens-like or reflecting properties, engineered to achieve specific frequency-dependent behaviors while maintaining a planar structure [67]. Importantly, the latter can be easily produced using materials like metal sheets or PCB (printed circuit board) technology, underscoring the practicality and accessibility of this transformative approach [68]. Furthermore, metasurfaces offer precise control over antenna polarization by being strategically positioned over designs, unlocking a plethora of possibilities such as linear to circular or linear to slanted polarization conversions [69, 70]. Additionally, by strategically integrating metasurfaces between antenna elements, designers can implement decoupling methods within arrays, effec-

tively mitigating unwanted resonances and providing a wide range of tailored solutions [71]. All techniques employ metasurfaces positioned between the near-field and far-field regions of the feeding antenna, facilitating precise manipulation of the radiated wave –a significant development endeavor. However, to further refine the radiating mechanism, integrating metasurfaces within the reactive near field of antennas becomes imperative. This integration actively governs antenna behavior, enabling deeper exploration of the potential of this combination. Termed "Metantennas," this integrated approach signifies the fusion of metasurfaces and antennas [7, 8, 61]. In metaantennas, metasurfaces are seamlessly integrated into the radiation mechanism, enabling, for instance, the creation of circular polarization at the antenna element level. This method also allows for the enhancement of properties such as bandwidth, gain, and modification of radiation pattern behavior [72–77]. A particularly noteworthy effect enabled by metantennas is the ability to miniaturize designs, allowing antennas to be smaller than their effective size. This results in achieving the same performance with a slightly smaller radiating element, thereby improving efficiency, volume, material usage, and cost. Hence, metasurface concepts in antenna design can serve passive or active roles, depending on their placement. Positioned within the near-field to far-field region, they assume a passive role. Conversely, when integrated into the reactive-field region of the radiating antenna, they become active components.

On the other hand, metasurfaces can also be used to enhance the feeding mechanism for antenna elements and arrays, thereby improving bandwidth performance and efficiency. This enhancement contributes to the development of high-quality, low-loss corporate feeding structures [64, 78]. For instance, the gap waveguide (GW) feeding technology [79] was introduced in the last decade to surpass the requirement for electrical contact among different layers of rectangular waveguide array antennas. The GW feeding employs a metasurface that mimics a perfect magnetic conductor (PMC) to control the propagation of electromagnetic waves inside the gap between parallel metal plate waveguides [79, 80]. Unlike conventional planar transmission lines like microstrip and coplanar lines, GW boundary conditions prohibit unwanted electromagnetic coupling or leakage, thereby improving energy efficiency. Furthermore, the engineered effective index of the metasurface allows for antennas with reduced dimensions. This concept was a breakthrough that enabled improved integration levels and inspired several new compact planar array antenna designs with low-sidelobes and ultra-widebands, for single and dual-polarized radiation patterns [50, 81, 82]. Despite these achievements, current GW technologies are limited to using the metasurface only in the feeding section, typically relying on a certain integration allowance to feed a proper radiating element. Such conditions often necessitates the use of multilayer schemes to meet the requirements for bandwidth and standing-wave operation [83], making it challenging to achieve higher levels of integration.

In this work, we present an approach that utilizes a bed of pins to develop a GW feeding mechanism, directly coupled to the radiating layer via slots. Our idea simplifies the integration of guided-to-radiating electromagnetic mode transitions in the antenna fabrication process, a technique previously proven effective in antenna design [80]. Departing from conventional parallel plate radiating elements, which typically exhibit well-separated Fabry-Perot resonances, we incorporated a bed of pins on both internal faces of these elements. This proposal demonstrates a broader spectrum

of modes, significantly expanding the antenna's operational bandwidth. Moreover, we simultaneously obtained both perfect electric conductor (PEC) and perfect magnetic conductor (PMC) cavities within the same system by employing a bed of pins on both parallel plates. This enabled efficient operation for frequencies lying between the corresponding electric and magnetic Fabry-Perot resonances of the metasurface-based parallel plate radiator. Importantly, our metasurface-based antenna design is entirely metallic, contrasting with prior approaches that integrate dielectric components. This deliberate choice stems from the recognized reduction in energy efficiency associated with dielectric elements due to their high levels of dielectric losses. Compared with available literature, our concept has several advantages, including a more compact design, single-layer feeding, high polarization purity, higher gain levels, broader bandwidths, highly efficient design, and easy-to-scale antenna array. All these advantages make our idea suitable for demanding applications such as Active Electronically Scanned Array (AESA) Radars and single-polarized satellite systems. Despite the potential bulkiness introduced by the incorporation of parallel plates compared to conventional slot antennas, the trade-off is justified by the superior quality and directive nature of the pencil beam it emits. Notably, our design achieves an impressive gain advantage of approximately 2 dBi per element over standard slot radiating elements, making it compatible with phased array systems. This feature enhances its versatility and opens up new opportunities for innovation in modern antenna design.

## 5.2 Antenna Element Design

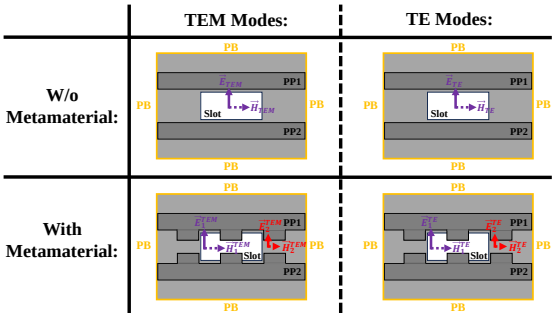



Figure 5.1: *Pictorial depiction of TEM and TE modes in the systems without (top panel) and with (bottom panel) metasurfaces.*

### 5.2.1 Concept

Leveraging the insights from the GW theory [79, 80], we comprehend its essence as an interplay of hard and soft surfaces. This phenomenon typically materializes in waveguides composed of parallel plates with a bed of nails positioned exclusively on one side of the plates, as illustrated (for a single nail) on the left side of Figure 5.2(a). The plate adorned with the bed of nails serves as a high-impedance surface, emulating a PMC, and is designated as the hard surface. In contrast, the opposing flat metal surface, characterized as a PEC, is labeled the soft surface. In this latter configuration, the propagation of electromagnetic modes is impeded when the distance between

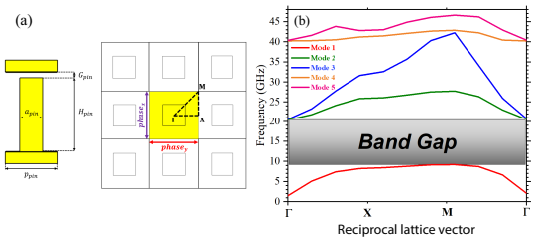



Figure 5.2: *(a) Schematic representation of a unit cell of the PEC-PMC cavity and (b) the corresponding PBG profile.*

the bed of nails and the opposite flat plane is less than a quarter wavelength ($\lambda/4$) at the central frequency. The latter is numerically shown by the photonic bandgap (PBG) in Figure 5.2(b), calculated for $a_{pin} = 2mm$, $H_{pin} = 6mm$, $G_{pin} = 1mm$, and $p_{pin} = 4.5mm$. Recognizing the nonexistence of naturally occurring PMCs, the artificial surface providing PMC boundary conditions is conventionally referred to as a metasurface. Drawing inspiration from this principle, we hypothesize that by incorporating the metasurface concept into both parallel plates, we can intricately tailor and fine-tune the propagation modes through the corresponding PBGs of the periodic structures. In particular, we envision that by implementing this concept into the radiating element, we can effectively enhance the operating bandwidth of a conventional parallel-plate antenna array.

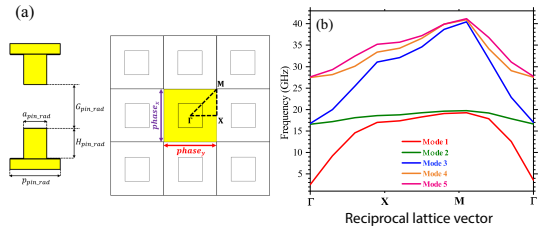



Figure 5.3: *(a) Illustrative representation of the unit cell of a metasurface-based cavity and (b) the corresponding PBS.*

To elucidate our proposal, we commence with a comparative illustration of the cross-section of the radiating element in Figure 5.1. Two distinct configurations take center stage: one integrates the waveguide concept of parallel plates without (w/o) metasurfaces, and the other incorporates metasurfaces. In both scenarios, the visually represented TEM (transverse electromagnetic) and TE (transverse electric) excitation modes employ a slot as a conduit to efficiently feed the radiating element. For the system w/o metasurfaces, we can initially assume that the parallel plates extend infinitely. Within this framework, the system behaves as a Fabry-Perot resonator (FPR) with resonant frequencies determined by the expression

$$f_0 = \frac{nc}{2d}, \quad \text{for} \quad n = 1, 2, 3, \ldots \tag{5.1}$$

where $d$ denotes the separation between the conductive planes, whilst $n$ and $c$ represent the mode number of the FPR and the speed of light in vacuum, respectively. Conversely, assuming the parallel plates are again infinitely extended but now considering the presence of metasurfaces on both sides of the cavity, the determination of resonant

modes hinges on the photonic band structure (PBS) of the system. In this latter case, analytical expressions are elusive, and results can solely be derived through comprehensive full-wave electromagnetic simulations incorporating periodic boundary conditions (PBCs) around the unit cell of the metasurface, as illustrated in Figure 5.3(a). The numerical data presented in Figure 5.3(b) correspond precisely to the PBS for the system, calculated for a system with geometrical parameters $a_{\mathrm{pin_rad}} = 2.2mm$, $G_{\mathrm{pin_rad}} = 5.1mm$, $p_{\mathrm{pin_rad}} = 4.9mm$, $H_{\mathrm{pin_rad}} = 2.95mm$. Importantly, these results reveal the absence of inhibited frequency bands, commonly referred to as band gaps (BGs), across the entire frequency range. The latter is due to the occurrence of multiple modes in the structure, as it can be seen from the overlap of the operating frequencies for modes 1 to 5 in Figure 5.3(b).

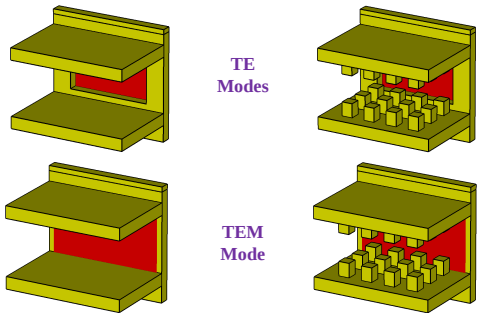



Figure 5.4: *Depiction of the TE (top panel) and TEM (bottom panel) feeding modes in the systems without (left-hand side) and with (right-hand side) metasurfaces.*

The operating frequency band in this work spans from 10 GHz to 18 GHz. The focus of our study transitions to the utilization of the proposed PPs as the radiating elements, as depicted in Figure 5.4. Initially, we conduct simulations on the PPs, exploring their behavior when fed by TE and TEM modes. This investigation is performed in two scenarios: one without metasurfaces and another with metasurfaces, as illustrated by the top images in Figure 5.4. The TE modes are introduced into the system through a meticulously designed slot radiating element. In contrast, the TEM modes are directly injected into the PPs region, bypassing consideration of the waveguide modes in the source region. This distinction is visually represented by a larger slot area, highlighted in red, in comparison to the TE modes feeding. Since we are interested in a high-gain antenna array design, periodic boundary conditions (PBCs) are employed along the lateral dimensions of the radiating unit cell in Figure 5.4. The dimensions of the slots are configured with a width and height of 12.5mm and 8mm, respectively, to have the PP features in a highly compact design. Numerical simulations for the $S_{11}$ parameter are shown in Figures 5.5(a) and 5.5(b) for the systems without and with metasurfaces, where results for the TEM and TE modes are presented by solid and dashed lines, respectively. These results are shown for different separations ($d$) between the PPs.

In Figure 5.5(a), the TEM mode (depicted by solid lines) within the PPs (without metasurfaces) clearly exhibits a lack of cut-off frequency, showcasing broadband impedance matching above 13GHz. The latter suggests a near-perfect approximation of the wave impedance within the PPs to 377 Ohms, effectively minimizing reflections back to the source and ensuring an efficient radiation process. In contrast, the

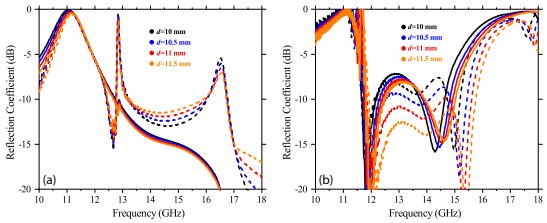



Figure 5.5: *Results are shown for the system a) without and b) with the bed of pins. Solid and dashed lines are for the TEM and TE ports, respectively. The insets in (a) and (b) are used to indicate that black, blue, red, and orange curves are for* $d = 10$ *mm,* $d = 10.5$ *mm,* $d = 11$ *mm, and* $d = 11.5$ *mm, respectively.*

TE modes (illustrated by dashed lines) guided within the PPs environment experience reflections due to the unmatched wave impedance between the input mode and the PP waveguide. Indeed, the TE modes forced within the PPs experience a robust reflection peak induced by an impedance mismatch around 16.7 GHz. It is noteworthy that both TEM and TE modes exhibit a FP resonance around 13 GHz. This resonance aligns well with Eq. (5.1) (with $f \in [13\text{ GHz}, 15\text{ GHz}]$ for $d \in [10\text{ mm}, 11.5\text{ mm}]$) for a hypothetical PEC cavity (i.e., considering infinite PEC flat plates). On the other hand, the outcomes in Figure 5.5(b) unveil the emergence of a higher-frequency resonance for both TEM and TE modes with the addition of metasurfaces on both PPs (illustrated in the right panel of Figure 5.4). Simultaneously, the initial resonance subtly shifts to a lower frequency (from $\sim$ 13 GHz to $\sim$ 12 GHz). As the bed of nails on both PPs mimics PMCs, the newfound higher-frequency resonance can be regarded as a FP resonance in a PMC cavity. While there exist analytical expressions for FP resonances in ideal PMC flat cavities [84], we lack the means to derive equations for the effective width, permittivity, and permeability of the emulated PMC cavity with metasurfaces. Therefore, in contrast to Eq. (5.1), we cannot formulate an equation to delineate the higher-frequency FP resonance in Figure 5.5(b).

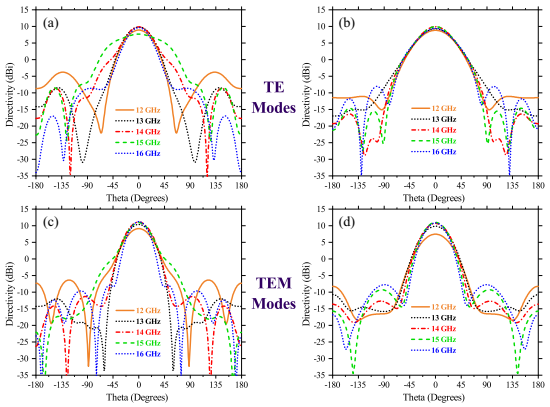



Figure 5.6: *Far-field radiation patterns for (a)-(b) TE and (c)-(d) TEM modes. Data is comparatively presented for the antenna with pins in (a) and (c), and without pins in (b) and (d). Simulations were carried out for frequencies ranging from 12 GHz to 16 GHz, as shown in the insets.*

Despite a slight narrowing of the impedance-matched band (for both polarizations) in the system with metasurfaces, resulting from the effective hybridization of PEC

and PMC FP resonances within the radiating element (refer to Figure 5.5(b)), numerical data in Figures 5.6(a)-(b) and Figures 5.6(c)-(d) indicate an enhancement in the system's directivity for TE and TEM modes, respectively. These results are comparatively shown for five different frequencies, namely 12 GHz, 13 GHz, 14 GHz, 15 GHz, within the impedance-matched frequency band. In particular, Figures 5.6(a)-(c) (Figures 5.6(b)-(d)) show numerical results for directivity of the radiating element with (w/o) metasurfaces.

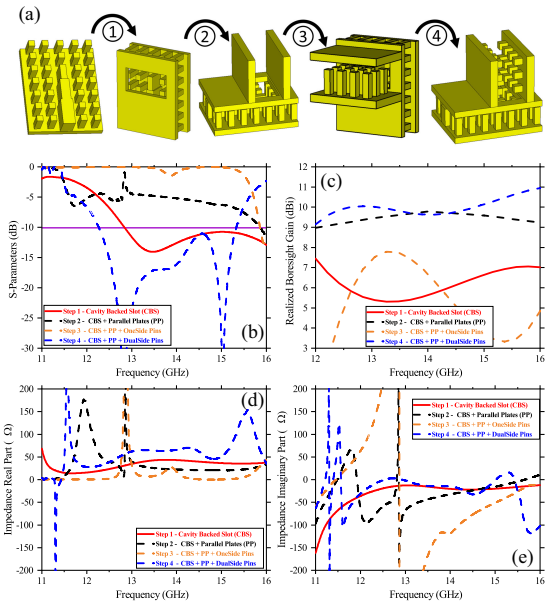



Figure 5.7: *(a) Successive steps to prototype the antenna in this work: 1) a cavity back slotted (CBS) radiator; 2) CBS + parallel plates resonator; 3) CBS + parallel plates resonator with pins on one side; 4) CBS + parallel plates resonator with pins on both sides. Numerical results from full-wave electromagnetic simulations are shown for the (b) S-Parameters and (b) Boresight gain associated to each one of the prototyping steps in (a).*

## 5.2.2 Integrated Gap-Waveguide Parallel Plate Design

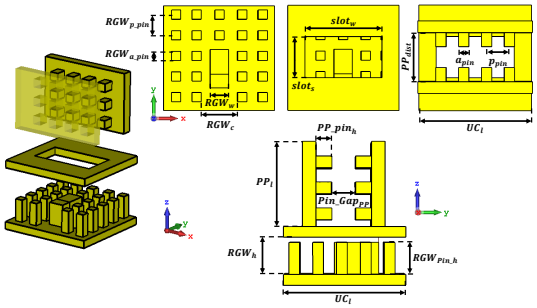



Figure 5.8: *Parametric view of the antenna radiating element. The design parameters are* $RGW_{\mathrm{p_pin}} = 4.5$ *mm,* $RGW_{\mathrm{a_pin}} = 2$ *mm,* $RGW_{\mathrm{w}} = 4$ *mm,* $RGW_{\mathrm{c}} = 8$ *mm,* $slot_{\mathrm{w}} = 17$ *mm,* $slot_{\mathrm{s}} = 9$ *mm,* $PP_{\mathrm{dist}} = 10.5$ *mm,* $a_{\mathrm{pin}} = 2.2$ *mm,* $p_{\mathrm{pin}} = 4.9$ *mm,* $UC_{\mathrm{l}} = 23.5$ *mm,* $PP_{\mathrm{l}} = 16$ *mm,* $RGW_{\mathrm{h}} = 7$ *mm,* $PP_{\mathrm{pin_h}} = 3$ *mm,* $Pin_{\mathrm{Gap_PP}} = 4.5$ *mm and* $RGW_{\mathrm{Pin_h}} = 6$.

Upon finalizing the design of the radiating element, our focus shifted to implementing a gap waveguide transmission line for the feeding mechanism. Specifically, each slot is meticulously connected through a probe, culminating in a cavity-backed slot antenna configuration. A noteworthy aspect is the transition from the probe to the slot, enabling the seamless feeding of parallel plates and resulting in an impressively compact radiating mechanism. The systematic design of the radiating unit cell is illustrated in Figure 5.7(a). The corresponding $S$ parameters, boresight gains, and impedance (both real and imaginary parts) behavior at each design step are presented in Figures 5.7(b), 5.7(c), 5.7(d), and 5.7(e), respectively. Notably, in Step 3, the reflection is considerably high due to the soft-hard boundary conditions. These conditions create an environment where the real impedance approaches zero, effectively preventing any mode propagation within the system. In contrast, Step 4 reveals a series of impedance-matched resonances for the two-cavity system, demonstrating a marked improvement in performance. The real and imaginary parts of the impedance curves further illustrate how the multi-resonant scheme can be achieved. When the imaginary part of the impedance is almost zero and fluctuates within the frequency band of interest, the real part can be matched and stabilized around 50 Ohms. Figure 5.8 showcases the set of geometrical parameters for the designed radiating device, with their corresponding numerical values provided in the caption.

To further elaborate on the dual-cavity aperture behavior, Figure 5.9 shows the electric field distribution across multiple planes in the radiating section, specifically: 1) Slot XY-plane, 2) XY-plane, 3) XZ-plane, and 4) YZ-plane. This visualization demonstrates how the behavior of these field lines aligns with the generated patterns shown in Figure 5.6. The feeding section is also included in this overview, illustrating how the main beam and corner refraction contribute to the creation of the radiation pattern. The electric field (E-field) is plotted for two different observation points: when its components are real ($\Phi = 0°$) and when they are imaginary ($\Phi = 90°$). Notably, the E-field distribution at 12 GHz and 15 GHz, as well as at 13 GHz and 14 GHz, shows how the dual-cavity aperture using pins can bring multiple close resonances together, effectively widening the bandwidth of the radiating element. For the 15 GHz E-field distribution, it is evident that the line pattern is broader than at other frequencies, as the field escapes the parallel plate region. This results in a broader radiation pattern and a drop in directivity, which helps to widen the overall radiation pattern.

### 5.2.3 Simulated Results

To enhance understanding of the operational principles, we conducted simulations of the antenna element unit cell across various scenarios through the commercial software CST Microwave Studio. These included a single-element radiating antenna, as well as linear or planar arrays achieved through the implementation of periodic boundaries in one or both directions along the unit cell plane, as illustrated in Figure 5.10(a). When simulated under periodic boundaries (PBs), the active Voltage Standing Wave Ratio (VSWR) of the unit cell was considered instead of the real element unit cell in the array. Four distinct scenarios were examined in the simulations, as depicted in Figure 5.10(a), each labeled according to the utilization of PB and/or OB (open boundaries) boundary conditions. Specifically, the first scenario employed OBs si-

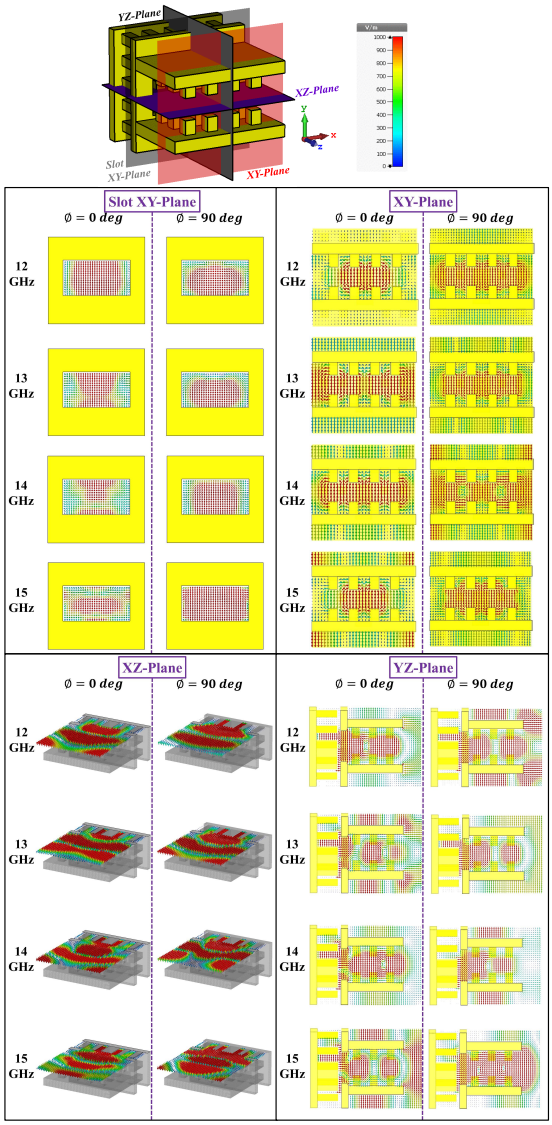



Figure 5.9: *Numerical results illustrating the variation of the electric field distribution across multiple observation planes within the specified frequency band. Each plane offers a detailed view of how the electric field changes at different positions, providing significant insights into the field's behavior and characteristics over the frequency range.*

multaneously along the $x$- and $y$-axes (labelled OB all), while the second and third scenarios alternated PBs and OBs along the $x$ (PP-Active) and $y$ (Y-Active) directions, respectively. The fourth scenario involved PBs simultaneously along the $x$- and $y$-axes (labelled PB all-Active), as schematized. The corresponding $S_{11}$ parameter was calculated and comparatively plotted in Figure 5.10(b) for all cases. Additionally, the figures of merit, defined as boresight gain, azimuth half-power beam-width (A-HPBW), and elevation half-power beam-width (E-HPBW), are shown in Figure 5.11. Analysis of these results reveals that the reflection coefficient reaches 26.24% (11.72 GHz–15.26 GHz) for the first scenario, where the first resonance is broader than the second. This behavior arises from the usage of metasurfaces, which induce the combination of two modes. A deeper understanding of the last phenomenon is facilitated by examining the pattern parameters in Figure 5.11. Notably, a variation in behavior occurs at

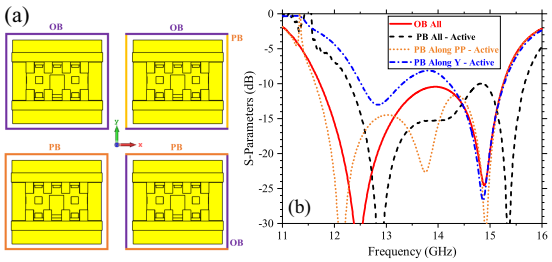



Figure 5.10: *(a) Description of the simulated element boundary conditions and (b) the related reflection coefficient results under each circumstance.*

approximately 13.5 GHz, causing the mode inside to become more directive, resulting in a broader E-HPBW, which decreases to an average of 50 degrees at 14 GHz. Despite the significant drop in E-HPBW, the increase in A-HPBW suggests the influence of the hidden mode within the broader resonance.

In the second scenario, where PB along PP-Active are considered, we observe the emergence of three resonances. This indicates a split in the broader behavior previously noted. This active case serves as an example of the unit-cell's application in a linear array configuration. The reflection coefficient in this case reaches 27% (11.63 GHz-15.26 GHz). Examining the pattern parameters, it can be noted a stable performance around 8 dBi for boresight gain within the region containing the first two mode resonances. This stability is reflected in a slight decrease in the A-HPBW, which corresponds to the pattern associated with the PB orientation along the PPs. Additionally, we observe a stable variation in the E-HPBW, with a smooth transition from wider to narrower beam widths. These results suggest that the first and second resonances share the same mode nature, indicating that the mode inside remains consistent but with different cut-off frequencies. These modes are generated by both the PP (PEC plates) and the emulated PPs (PMCs plates) created by the pins. Furthermore, an intrinsic resonance occurs within the structure, leading to a drop in the boresight gain at 14.3 GHz, which subsequently broadens the A-HPBW. This is followed by the emergence of a highly directive mode observed at 14.9 GHz, resulting in a severe narrowing of the A-HPBW.

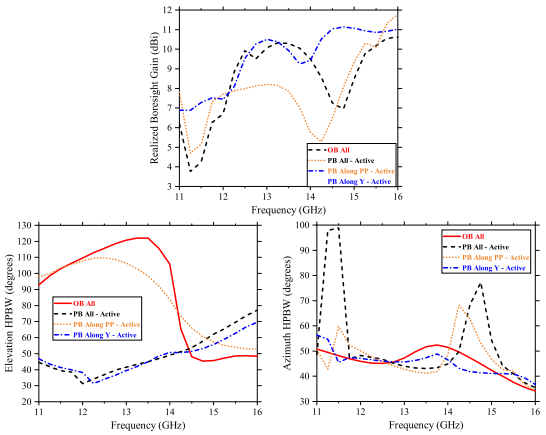



Figure 5.11: *Overview on some radiation pattern figure-of-merit evolution aligned to each applied boundary conditions in the simulated element.*

Regarding the third case, which involves the use of PB along Y-Active, we observe a significant impact on the matching of the unit cells, resulting in a notable reduction and suppression of the two modes responsible for the broader first resonance observed previously. However, the second resonance remains strong due to its dominant nature. In this active linear array solution, we note significant changes primarily in the E-HPBW, as the array factor is now related to this axis. The previously observed broad E-HPBW is now reduced within the bandwidth of interest, with variations observed at 12.25 GHz and 14 GHz. Notably, the predominant behavior for the E-HPBW differs from the previously observed pattern, as it gradually broadens over frequency, directly impacting the realized gain, which is significantly improved with this arrayed selection. Furthermore, a higher directivity is observed in the unit cell's behavior. Finally, in the fourth case, we present the solution of the unit cell using PB All-Active, which is particularly significant as it demonstrates the proposed concept when developing a planar array configuration as an antenna. In this specific case, we observe a combination of both the second and third scenarios, which is clearly evident in the pattern parameters and the reflection coefficient. Regarding impedance behavior, we note that the resonances are shifted to higher frequencies due to the unmatched behavior caused in the third case, leading to a slight increase in reflection levels. The achieved bandwidth is 24.2% (12.29 GHz-15.67 GHz), which is still satisfactory, although further impedance transformation will be necessary, specifically for this case when implemented in the antenna. Furthermore, analyzing the pattern parameters, we observe that the tendencies of both the second and third modes are directly evident, indicating similar behavior for the E-HPBW and A-HPBW, with only slight differences. In the E-HPBW, the significant variation is shifted to 12 GHz, and a more stable performance is achieved in the rest of the bandwidth. For the A-HPBW, there is a tendency toward higher frequencies, reflecting the insertion of elements in the other direction, which modifies the pattern of the wave predominantly polarized in the azimuth/horizontal direction. Additionally, in the boresight gain, we observe that the overall performance aligns with both cases, and the drop at approximately 14 GHz is more pronounced in the combination, which has also shifted to higher frequencies, coinciding with the position of the inner resonance masked in the reflection coefficient.

## 5.3 4x4 Antenna Array Design

### 5.3.1 Feeding Network

Upon completion and optimization of the antenna element design, we progressed to demonstrate the concept and implementation by integrating the element into a planar antenna array configured as a $4 \times 4$ array. Given that the antenna element already encompasses feeding and matching integration, our challenge shifted to designing a complex feeding network capable of providing each element with the necessary phases and amplitudes. To enhance the feeding technique and align with the input port of the antenna element, we also employed the concept of gap waveguide to construct the entire feeding network. Our aim was to feed all elements with maximum accuracy in amplitude and phase to ensure a beam pointing towards the boresight direction. Achieving this required minimizing discrepancies in amplitudes and phases across all

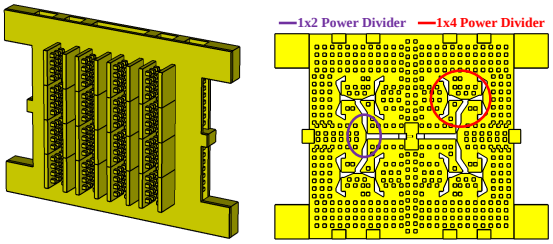



Figure 5.12: *Viewing of external and internal designed antenna model comprising radiation and signal layers. On left side, the 3D model of the full 4x4 proposed array and on right side, the signal distribution portraying the designed power dividers .*

elements. In Figure 5.12, we present a 3D schematic of the final $4 \times 4$ planar array. The left side illustrates the complete scheme, while the right side showcases the gap waveguide feeding network with the Rad PP and top GND (Ground Plane) removed for demonstration purposes. For the planar array environment, we chose an element-to-element spacing of 22.5 mm, approximately corresponding to $\lambda_0$ at the center of the operating frequency range. Given that parallel plate designs utilizing an all-metal concept typically result in unit cell sizes comparable to the wavelength, careful attention was paid to minimize the generation of grating lobes. Optimal element spacing was sought to balance and optimize the parallel plates, ensuring lower grating lobes and minimizing array side-lobe levels (SLL). Developing these complex feeding networks posed challenges in achieving wideband behavior covering the entire antenna element operating bandwidth while maintaining stable performance in amplitude and phase across each element. To address this, each transition and component of the feeding network was optimized to minimize reflection coefficients and ensure stable transmission coefficients. Power dividers required careful optimization, employing techniques such as tapered transitions to produce smooth impedance transformation. By cascading each component of the feeding network with low input reflections, we achieved a high-quality feeding network capable of effectively feeding the radiating component.

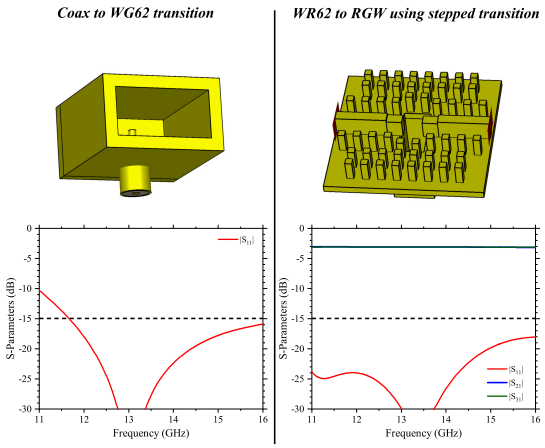



Figure 5.13: *Simulated results from the transitions required on the design to enable a measuring interface for the prototype antenna model.*

In Figure 5.13, we showcase the initial two steps of the feeding network. On the left

side panel, we illustrate a Coax to WR62 waveguide transition, featuring inner dimensions of 15.8 mm×7.9 mm. This component serves as a prototype user interface for post-manufacture device measurement. While this transition offers a degree of wideband capability, it is constrained by waveguide cut-off modes, leading to limitations in reflection levels. We optimized this component to achieve reflection levels of at least -15 dB across the entire impedance bandwidth. On the right side panel, we show a transition from WR62 to groove gap waveguide, implemented as a vertical power divider. A stepped transitions was used to facilitate impedance transformation and ensure efficient power flow throughout the feeding network, optimizing its performance. The top ground layer is hidden to clearly show our idea. The objective for this component was to achieve reflection coefficient levels of at least -20 dB. By vertically dividing power as per the proposed method, we ensure that the phases of each port differ by 180 degrees. Within the gap waveguide layer, the pins were optimized to establish the correct bandgap, facilitating the flow of modes within the desired bandwidth. The last process follows the mechanism demonstrated in Figure 5.2, where the dispersion diagram is plotted across the entire Brillouin zone. The bandgap was precisely engineered within the 9 GHz to 20.5 GHz bandwidth to enable precise feeding of the radiator element, as discussed earlier.

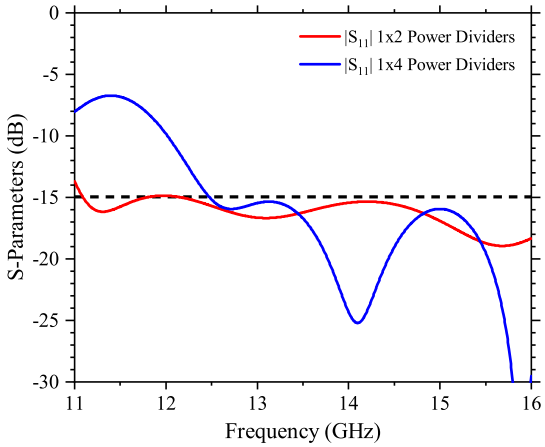



Figure 5.14: *Reflection coefficient simulated results for the different designed power dividers located in the GW signal layer.*

To delve into the performance of the feeding network, reference should be made to Figure 5.12, where the $1 \times 2$ and $1 \times 4$ power dividers are highlighted. To maintain broad bandwidth while minimizing reflection, we applied a standard transformation with tapered behavior. In the $1 \times 4$ divider, two sequential transformations were necessary due to element proximity, making it more critical for compactness. Additionally, a groove tilt was introduced to enhance compactness, albeit causing slight power distribution imbalance among the elements. Despite this, the design remains compact and aligns with element spacing sizes. Figure 5.14 illustrates the reflection coefficient performance for both dividers. The $1 \times 2$ divider demonstrates stability below $-15$ dB across the entire bandwidth. Conversely, the $1 \times 4$ exhibits improved performance above $12.5$ GHz, achieving reflections below $-15$ dB. Further optimization post-divider integration enhanced system performance, evident in subsequent full antenna simulations. It's noteworthy that to mitigate the $180$–degree phase imbalance

introduced by the central vertical power divider in the gap waveguide layer, the $1 \times 4$ dividers were mirrored concerning the array's center, enabling compensation for this phase shift in both slots and parallel plates.

### 5.3.2 Prototype

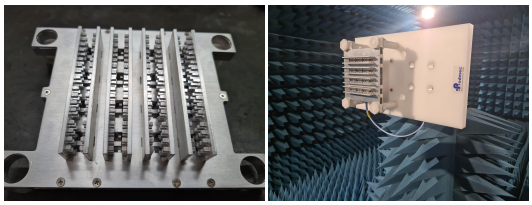


Figure 5.15: *Prototype viewing of the proposed antenna. Top view with the radiation aperture and 3D-view in the anechoic chamber ready for measurements.*

The prototype, shown in Figure 5.15, was crafted using a CNC (Computer Numerical Control) milling machine. To facilitate mounting, the radiator PP with metamaterial pins was fabricated in separate pieces. However, challenges arose during the prototyping phase, particularly regarding the assembly of these components. Unlike conventional PP designs, which are typically manufactured as single units, our approach necessitated separate production to incorporate the metamaterial pins. Consequently, precisely inserting these PPs into the horizontal GND plane at a precise 90-degree vertical orientation proved to be a significant challenge, requiring meticulous attention to detail to minimize errors. Another noteworthy issue was the necessity of securely affixing these PPs within the horizontal top GND. To address this, a solution was devised involving the creation of a smaller slot in the top GND and a corresponding tooth-like structure on the PPs. This enabled a snug fit between the two components, with the teeth being hammered into the slot to ensure a secure connection. However, a drawback of this solution was the need for the slot to be slightly larger than the teeth, resulting in small unfilled areas between the components. This discrepancy led to minor current instabilities in the vicinity, particularly notable due to the presence of the ridge gap waveguide in the layer below. Despite the high precision achieved during the prototyping process, this solution contributed to resonance shifts, as demonstrated in Figure 5.16. Notably, the red circles highlight imperfections in the fit between the teeth and the slot, underscoring the impact of fabrication errors on performance. Future endeavors can explore various avenues to address fabrication errors in the radiating component. For instance, one viable approach entails applying conductive glue in the affected regions, thereby reducing the slot area and alleviating the current discontinuity issue. Alternatively, fabricating the entire piece from a single aluminum block using a 3D-axis CNC machine offers another promising solution. While less conventional, this method could enable precise cutting of the block in every axis, yielding a final piece of exceptional accuracy.

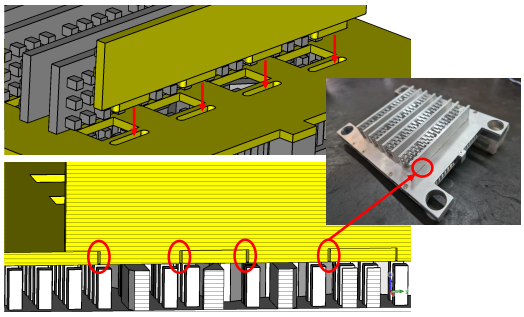


Figure 5.16: *Demonstration of the situational concern in regards of the mounting method of the prototype, related to the divergence in the measured parameters.*

## 5.4 Simulation and Measurements

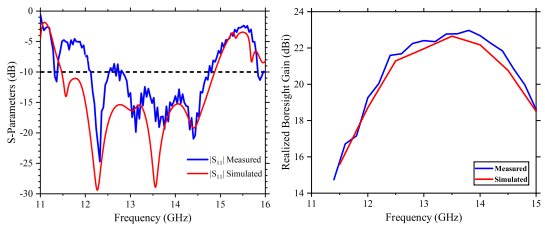



Figure 5.17: *Comparison between simulated and measured S-parameters and Realized Boresight Gain of the proposed antenna concept.*

A comparison between the simulated and measured results of the manufactured antenna array prototype is presented in Figures 5.17(a)-(b). The simulated reflection coefficient achieves an operational bandwidth of 26.1% considering VSWR$<$2 (see Figure 5.17(a)), whereas the measured result achieved 20.9%. It is worth noting that while the behavior of the resonances could be accurately predicted, fabrication errors and tolerances caused some resonances to shift slightly in frequency (as previously discussed), directly impacting the narrowing of the measured impedance bandwidth. Simulated and measured boresight gain varied between 15.2 dBi and 22.9 dBi (see Figure 5.17(b)). The high directivity of the antenna elements used in the array contributes to overall device performance, resulting in a more stable and high-gain pencil-beam. Minor discrepancies between simulated and measured results are apparent, largely attributable to the all-metal design principle. These findings highlight the feasibility of our concept in designing highly efficient, compact, and directional antennas with minimal energy loss. Specifically, the averaged radiation efficiency reached approximately 97.5%, while the total efficiency averaged 96% across the entire operational bandwidth.

Normalized radiation patterns at 12 GHz, 13 GHz, and 14 GHz are shown in Figures 5.18(a)-(f), showcasing the high accuracy of predicted co-polarization radiation patterns. The measured SLL for these specific patterns were $-10.5$ dB, $-13.8$ dB, and $-11.9$ dB for the $\phi = 0$ cut-plane, and $-11.2$ dB, $-15.1$ dB, and $-12.9$ dB for the $\phi = 90$ cut-plane, respectively.

Table 5.1: *Performance Comparison among Metal Antennas with GW feeding network*

| **Designs** | **Frequency Band (GHz)** | **Array Size** | **Number of Layers** | **Imp. BW (%)** | **Gain (dBi)** |
|---|---|---|---|---|---|
| Ref. [85] | 23-30.5 | 8x8 | 2 | 28 | 20.5-26.4 |
| Ref. [86] | 56-65.7 | 16x16 | 2 | 16 | >32.5 |
| Ref. [87] | 18.8-30.3 | 8x8 | 2 | 46.8 | 24.3-27.7 |
| Ref. [88] | 12-15 | 2x2 | 1 | 21 | 12.2-13.8 |
| **This work** | 12-14.8 | 4x4 | 1 | 20.5 | 15.2-22.9 |

Table 5.2: *Performance Comparison among Metantennas*

| **Designs** | $f$ **(GHz)** | **Array Size** | **Feeding Technology** | **Imp. BW (%)** | **Peak Gain (dBi)** | **App. Eff. (%)** |
|---|---|---|---|---|---|---|
| Ref. [89] | 60 | 8x8 | SIW | 15.4 | 24.9 | <49.4 |
| Ref. [90] | 5.5 | Single Element | Microstrip Line | 24.5 | 7.8 | Not Calculated |
| Ref. [91] | 34 | 4x4 | SIGW | 35.5 | 17.4 | <30.2 |
| Ref. [92] | 3.5 | 2x2 | Microstrip Line | 17.8 | 11.9 | <45.3 |
| **This work** | 13.5 | 4x4 | RGW | 20.5 | 22.9 | <89 |

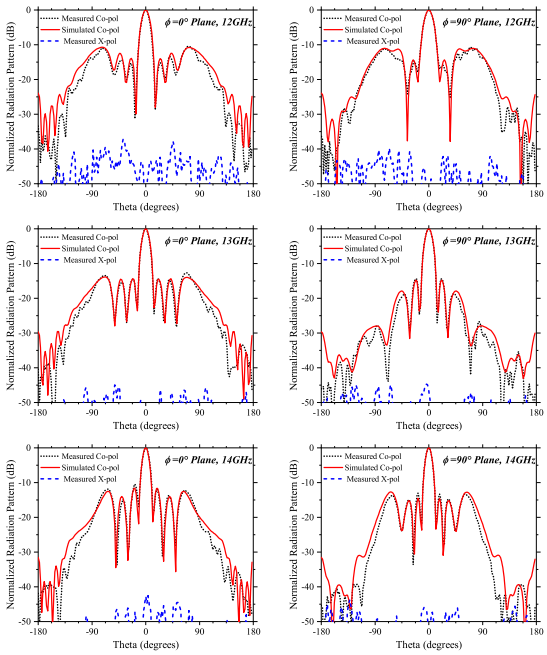



Figure 5.18: *Comparison between simulated and measured radiation patterns for both farfield cut sections: azimuth and elevation, demonstrated at different frequency points.*

## 5.5 Comparison with the State-of-the-Art Design Concepts

The Cross Polarization Ratio (CPR) serves as a quantification of the dominance of the co-polar pattern over the cross-polar pattern at specific azimuth and elevation angles. Essentially, it acts as a metric for assessing the linear polarization purity of an antenna prototype, with higher CPR values indicating greater purity. In an ideal scenario,

such as with a theoretical rectangular slot antenna, cross-polarization values are expected to be minimal, resulting in a high CPR, which is indicative of high polarization purity. However, practical constraints often limit our ability to precisely measure these extremely low levels of cross-polarization. Environmental factors, including scattering within the measurement chamber, can contribute to increased cross-pol values, sometimes averaging around $-30$ dB. This phenomenon was observed in our study, where despite the anticipated high polarization purity facilitated by the slot and parallel plate design, cross-pol values averaged around $-45$ dB at boresight. Nonetheless, this outcome still signifies a high CPR, highlighting the antenna's capability to maintain polarization purity under real-world measurement conditions. Additionally, we compared our proposed idea with previously reported antennas utilizing metal technology and integrated metamaterial-based solutions. The performance of various antenna characterization parameters is summarized in Tables 5.1 and 5.2.

Upon comparing with the references listed in Table 5.1, it becomes apparent that despite the increased size of the prototype –achieving an aperture volume of $90$ mm $\times$ $90$ mm $\times$ $27.5$ mm and ensuring a maximum aperture efficiency of 89%–the impedance bandwidth could be maintained at a comparable level. Furthermore, the realized boresight gain related to the array can be increased, owing to the nature of the elements used. An advantageous aspect of this solution is its integration into a single-layer design, which effectively reduces the complexity of development. From Table 5.2, it is evident that the concept presented in this work achieves superior aperture efficiency compared to other metantennas. This superiority arises from the conventional use of PCB technology in state-of-the-art metantennas, emphasizing the absence of all-metal-based metantenna concepts in antenna array engineering.

## 5.6 Chapter Conclusions

Summarizing, this work presents a novel methodology for crafting highly integrable antenna array designs utilizing all-metallic metasurfaces. A key innovation lies in integrating metasurfaces directly into the radiating element to improve the impedance-matching, resulting in approximately 21% (12 GHz-14.8 GHz) bandwidth. Specifically, we introduce a mechanism akin to GW technology into the radiating element, which, as validated through numerical simulations and experimental measurements, yields a dual cavity exhibiting characteristics of both a PMC and a PEC, thereby showcasing electric and magnetic Fabry-Perot resonances. Importantly, this bandwidth expansion is achieved without compromising the high polarization purity expected from parallel plate-based antennas, as corroborated by experimental evidence. Furthermore, by integrating GW technology into both the feeding layer and the radiating metasurface-based parallel plates, we realize a highly compact all-metallic design boasting broad bandwidth, high gain (22.9 dBi), high polarization purity, and a stable radiation pattern.

# Chapter 6

# Conclusions and Future Work

In conclusion, this research has demonstrated how the integration of metamaterials, metasurfaces, and metaantennas is revolutionizing antenna design. These advanced materials provide unprecedented control over electromagnetic waves, enabling innovative solutions to traditional challenges. Their adaptability allows them to be effectively utilized in various regions and sections of an antenna, including the feeding network, reactive near field, near field, and far field. This versatility continually drives improvements, expanding the limits of conventional antenna performance.

Additionally, this study has underscored the creative freedom engineers have when designing and manipulating structures within the diverse antenna concepts explored in the literature. This flexibility not only broadens the scope of antenna design but also enhances the capabilities of state-of-the-art technologies. The incorporation of metamaterials into antenna design has unlocked a new realm of possibilities, fostering novel approaches and paving the way for groundbreaking discoveries.

To expand the applications of these engineered structures, we contributed to the international literature with three different works listed below:

- Chapter 2 presents the adapted content from a contribution in which we explored the use of an engineered purely dielectric chiral metasurface in the reactive near field of an elliptically polarized antenna with poor performance. The combination of the metasurface with the antenna significantly enhances its performance, transforming the elliptical polarization into circular polarization. This improvement not only addresses the previously observed narrowband situation but also broadens the polarization bandwidth and improves the reflection coefficient of the entire system. This is achieved by manipulating the wave within the chiral metasurface medium. Due to the limitations in finding a tool shop capable of manufacturing the proposed design in Brazil, the study remains theoretical. The evaluated scheme is fed by a Substrate Integrated Waveguide (SIW) feeding, making it ready for integration into an antenna array.
- Chapter 3 presents the adapted content of a contribution to the literature, focusing on the combination of the well-known ME-dipole with a superstrate, fed by a metasurface electromagnetic band-gap (EBG) structure, to create a UWB dual-polarized scalable antenna array. The proposed design integrates the dual-polarized scheme within a shared aperture tight dipole, making it a strong candi-

date for the radiation aperture concept. A key challenge was that the dual-layer feeding network, for each polarization, could not provide the bandwidth required by the radiating element. To address this issue, a hybrid metal+PCB Gap waveguide structure was adopted. This approach reduces field leakage and coupling in the corporate feeding network, thereby broadening the bandwidth and improving system efficiency by minimizing loss. The manufacturing of this project is planned as part of future work, representing a perspective for further development beyond this thesis.

- Chapter 4 contains the adapted content of a work focused on embedding a metasurface in the radiating aperture of a radiating element to manipulate the reactive near-field behavior and enhance its conventional performance. In a traditional parallel plate antenna, a single cavity enables a single Fabry-Perot resonance, depending on the environment used. In this upgraded version, the metasurface, represented by a bed of pins, is integrated into the parallel plate cavity environment, emulating a second cavity capable of generating a second Fabry-Perot resonance. This design demonstrated that the combination of these structures broadens the bandwidth while maintaining the high gain level characteristic of parallel plate designs and ensuring high-purity polarization in the radiated beam. The design was scaled to a $4 \times 4$ antenna array, with a feeding network also utilizing Gap waveguide technology to improve the corporate feeding design and response, consistent with the improvements observed in previous chapters. In contrast to the previous studies, this research was validated by a manufactured prototype, showcasing a strong match between theoretical analysis and experimental results.

As highlighted in this dissertation, future research in this field holds significant potential for advancements in performance, functionality, and efficiency, which could drive the development of the next generation of wireless communication and sensing technologies. A promising direction for future studies could be the evolution of the proposed metantenna concept to support dual polarization schemes, such as dual-linear, dual-slanted, and dual-circular polarization.

Given the rapidly growing demand for spectrum coverage in recent years —a trend expected to continue in the future— research focused on complex multi-band antenna designs would also be highly valuable. By combining multi-band capabilities with the concepts explored in this dissertation, it would be possible to create more compact and efficient antennas. Such designs would be well-suited for integration into next-generation mobile communication front-end antenna terminals, meeting the increasing needs for miniaturization and enhanced performance.

# References


[1] C. Balanis, *Advanced Engineering Electromagnetics*. Wiley, 2012. [Online]. Available: https://books.google.de/books?id=2eMbAAAAQBAJ

[2] K. B. Ng, H. Wong, K. K. So, C. H. Chan, and K. M. Luk, "60 ghz plated through hole printed magneto-electric dipole antenna," *IEEE Transactions on Antennas and Propagation*, vol. 60, no. 7, pp. 3129–3136, 2012.

[3] X. Ruan, "Designs of magnetoelectric dipoles in the millimeter-wave band," Ph.D. dissertation, City University of Hong Kong, 10 2019.

[4] T. Latha, G. Ram, G. A. Kumar, and M. Chakravarthy, "Review on ultra-wideband phased array antennas," *IEEE Access*, vol. 9, pp. 129 742–129 755, 2021.

[5] Y. Shi, G. Wang, Q. Liu, L. Guo, X. Zou, and H. Bai, "An ultrawideband compact magneto-electric dipole antenna and its coupled array," *IEEE Antennas and Wireless Propagation Letters*, vol. 22, no. 7, pp. 1662–1666, 2023.

[6] C. Balanis, *Antenna Theory: Analysis and Design*. Wiley, 2015. [Online]. Available: https://books.google.de/books?id=PTFcCwAAQBAJ

[7] C. Z. . Q. X. Liu, W.E.I., "Dispersion-engineered wideband low-profile metasurface antennas," *Front Inform Technol Electron Eng*, vol. 21, pp. 27–38, 2020.

[8] J. Wang, Y. Li, Z. H. Jiang, T. Shi, M.-C. Tang, Z. Zhou, Z. N. Chen, and C.-W. Qiu, "Metantenna: When metasurface meets antenna again," *IEEE Transactions on Antennas and Propagation*, vol. 68, no. 3, pp. 1332–1347, 2020.

[9] V. G. Veselago, "The electrodynamics of substances with simultaneously negative values of $\varepsilon$ and $\mu$," *Soviet Physics Uspekhi*, vol. 10, no. 4, p. 509, apr 1968. [Online]. Available: https://dx.doi.org/10.1070/PU1968v010n04ABEH003699

[10] J. B. Pendry, A. J. Holden, D. J. Robbins, and W. J. Stewart, "Low frequency plasmons in thin-wire structures," *Journal of Physics: Condensed Matter*, vol. 10, no. 22, p. 4785, jun 1998. [Online]. Available: https://dx.doi.org/10.1088/0953-8984/10/22/007

[11] J. Pendry, A. Holden, D. Robbins, and W. Stewart, "Magnetism from conductors and enhanced nonlinear phenomena," *IEEE Transactions on Microwave Theory and Techniques*, vol. 47, no. 11, pp. 2075–2084, 1999.

[12] R. A. Shelby, D. R. Smith, and S. Schultz, "Experimental verification of a negative index of refraction," *Science*, vol. 292, no. 5514, pp. 77–79, 2001. [Online]. Available: https://www.science.org/doi/abs/10.1126/science.1058847

[13] S. Enoch, G. Tayeb, P. Sabouroux, N. Guérin, and P. Vincent, "A metamaterial for directive emission," *Phys. Rev. Lett.*, vol. 89, p. 213902, Nov 2002. [Online]. Available: https://link.aps.org/doi/10.1103/PhysRevLett.89.213902

[14] A. Dadgarpour, A. A. Kishk, and T. A. Denidni, "Gain enhancement of planar antenna enabled by array of split-ring resonators," *IEEE Transactions on Antennas and Propagation*, vol. 64, no. 8, pp. 3682–3687, 2016.

[15] W. Liu, Z. N. Chen, and X. Qing, "Metamaterial-based low-profile broadband mushroom antenna," *IEEE Transactions on Antennas and Propagation*, vol. 62, no. 3, pp. 1165–1172, 2014.

[16] J. Chen, S. Zhang, Q. Wang, L. Wang, G. Goussetis, and Q. Cheng, "Linearity and continuity enhanced phase shifter based on geometric-phase metasurface," *IEEE Transactions on Microwave Theory and Techniques*, vol. 72, no. 6, pp. 3614–3625, 2024.

[17] A. Noor and S. Koziel, "Dual-polarized wideband bandpass metasurface-based filter," *IEEE Antennas and Wireless Propagation Letters*, vol. 23, no. 1, pp. 404–408, 2024.

[18] E. Rajo-Iglesias, M. Ferrando-Rocher, and A. U. Zaman, "Gap waveguide technology for millimeter-wave antenna systems," *IEEE Communications Magazine*, vol. 56, no. 7, pp. 14–20, 2018.

[19] A. U. Zaman and P.-S. Kildal, *"GAP Waveguides," Handbook of Antenna Technologies*. Springer, 2016, no. Z. N. Chen et al.

[20] Z. Wu, L. Li, Y. Li, and X. Chen, "Metasurface superstrate antenna with wideband circular polarization for satellite communication application," *IEEE Antennas and Wireless Propagation Letters*, vol. 15, pp. 374–377, 2016.

[21] S. X. Ta and I. Park, "Low-profile broadband circularly polarized patch antenna using metasurface," *IEEE Transactions on Antennas and Propagation*, vol. 63, no. 12, pp. 5929–5934, 2015.

[22] Y. Huang, L. Yang, J. Li, Y. Wang, and G. Wen, "Polarization conversion of metasurface for the application of wide band low-profile circular polarization slot antenna," *Applied Physics Letters*, vol. 109, no. 5, p. 054101, 08 2016. [Online]. Available: https://doi.org/10.1063/1.4960198

[23] S. Niyamanon, R. Senathong, and C. Phongcharoenpanich, "Dual-frequency circularly polarized truncated square aperture patch antenna with slant strip and l-shaped slot for wlan applications," *International Journal of Antennas and Propagation*, vol. 2018, pp. 1–11, 07 2018.

[24] Y. Juan, W. Yang, and W. Che, "Miniaturized low-profile circularly polarized metasurface antenna using capacitive loading," *IEEE Transactions on Antennas and Propagation*, vol. 67, no. 5, pp. 3527–3532, 2019.

[25] M. S. Ellis, F. B. Effah, A.-R. Ahmed, J. J. Kponyo, J. Nourinia, C. Ghobadi, and B. Mohammadi, "Asymmetric circularly polarized open-slot antenna," *International Journal of RF and Microwave Computer-Aided Engineering*, vol. 30, no. 5, p. e22141, 2020. [Online]. Available: https://onlinelibrary.wiley.com/doi/abs/10.1002/mmce.22141

[26] K. Lu and K. W. Leung, "On the circularly polarized parallel-plate antenna," *IEEE Transactions on Antennas and Propagation*, vol. 68, no. 1, pp. 3–12, 2020.

[27] R. K. Mongia and P. Bhartia, "Dielectric resonator antennas—a review and general design relations for resonant frequency and bandwidth," *International Journal of Microwave and Millimeter-Wave Computer-Aided Engineering*, vol. 4, no. 3, pp. 230–247, 1994. [Online]. Available: https://onlinelibrary.wiley.com/doi/abs/10.1002/mmce.4570040304

[28] S. Fakhte, H. Oraizi, R. Karimian, and R. Fakhte, "A new wideband circularly polarized stair-shaped dielectric resonator antenna," *IEEE Transactions on Antennas and Propagation*, vol. 63, no. 4, pp. 1828–1832, 2015.

[29] R. Chowdhury, N. Mishra, M. M. Sani, and R. K. Chaudhary, "Analysis of a wideband circularly polarized cylindrical dielectric resonator antenna with broadside radiation coupled with simple microstrip feeding," *IEEE Access*, vol. 5, pp. 19 478–19 485, 2017.

[30] W.-J. Sun, W.-W. Yang, P. Chu, and J.-X. Chen, "Design of a wideband circularly polarized stacked dielectric resonator antenna," *IEEE Transactions on Antennas and Propagation*, vol. 67, no. 1, pp. 591–595, 2019.

[31] W.-W. Yang, W.-J. Sun, H. Tang, and J.-X. Chen, "Design of a circularly polarized dielectric resonator antenna with wide bandwidth and low axial ratio values," *IEEE Transactions on Antennas and Propagation*, vol. 67, no. 3, pp. 1963–1968, 2019.

[32] S. Gupta, A. Sharma, G. Das, R. K. Gangwar, and M. Khalily, "Wideband circularly polarized dielectric resonator antenna array with polarization diversity," *IEEE Access*, vol. 7, pp. 49 069–49 076, 2019.

[33] M. Bağmancı, M. Karaaslan, E. Unal, and F. Karadag, "Microstrip patch antennas covered with chiral metamaterial structures," 09 2018.

[34] Y.-w. Hu, Y. Wang, Z.-m. Yan, and H.-c. Zhou, "A high-gain circularly polarized fabry-perot antenna with chiral metamaterial-based circular polarizer," *Microwave and Optical Technology Letters*, vol. 62, no. 2, pp. 906–911, 2020. [Online]. Available: https://onlinelibrary.wiley.com/doi/abs/10.1002/mop.32102

[35] E. Hendry, R. V. Mikhaylovskiy, L. D. Barron, M. Kadodwala, and T. J. Davis, "Chiral electromagnetic fields generated by arrays of nanoslits," *Nano Letters*, vol. 12, no. 7, pp. 3640–3644, 2012, pMID: 22594393. [Online]. Available: https://doi.org/10.1021/nl3012787

[36] B. Orazbayev, N. Kaina, and R. Fleury, "Chiral waveguides for robust waveguiding at the deep subwavelength scale," *Phys. Rev. Appl.*, vol. 10, p. 054069, Nov 2018. [Online]. Available: https://link.aps.org/doi/10.1103/PhysRevApplied.10.054069

[37] F. R. Gómez, J. R. Mejía-Salazar, and P. Albella, "All-dielectric chiral metasurfaces based on crossed-bowtie nanoantennas," *ACS Omega*, vol. 4, no. 25, pp. 21 041–21 047, 2019, pMID: 31867495. [Online]. Available: https://doi.org/10.1021/acsomega.9b02381

[38] F. Reyes Gómez, O. N. Oliveira, P. Albella, and J. R. Mejía-Salazar,

"Enhanced chiroptical activity with slotted high refractive index dielectric nanodisks," *Phys. Rev. B*, vol. 101, p. 155403, Apr 2020. [Online]. Available: https://link.aps.org/doi/10.1103/PhysRevB.101.155403

[39] K. Wu, Y. J. Cheng, T. Djerafi, and W. Hong, "Substrate-integrated millimeter-wave and terahertz antenna technology," *Proceedings of the IEEE*, vol. 100, no. 7, pp. 2219–2232, 2012.

[40] Z. H. Jiang, Y. Zhang, J. Xu, Y. Yu, and W. Hong, "Integrated broadband circularly polarized multibeam antennas using berry-phase transmit-arrays for $ka$ -band applications," *IEEE Transactions on Antennas and Propagation*, vol. 68, no. 2, pp. 859–872, 2020.

[41] E. Prodan, C. Radloff, N. J. Halas, and P. Nordlander, "A hybridization model for the plasmon response of complex nanostructures," *Science*, vol. 302, no. 5644, pp. 419–422, 2003. [Online]. Available: https://www.science.org/doi/abs/10.1126/science.1089171

[42] P. Nordlander, C. Oubre, E. Prodan, K. Li, and M. I. Stockman, "Plasmon hybridization in nanoparticle dimers," *Nano Letters*, vol. 4, no. 5, pp. 899–903, 2004. [Online]. Available: https://doi.org/10.1021/nl049681c

[43] A. Vosoogh, M. Sharifi Sorkherizi, V. Vassilev, A. U. Zaman, Z. S. He, J. Yang, A. A. Kishk, and H. Zirath, "Compact integrated full-duplex gap waveguide-based radio front end for multi-gbit/s point-to-point backhaul links at e-band," *IEEE Transactions on Microwave Theory and Techniques*, vol. 67, no. 9, pp. 3783–3797, 2019.

[44] T. S. Rappaport, Y. Xing, G. R. MacCartney, A. F. Molisch, E. Mellios, and J. Zhang, "Overview of millimeter wave communications for fifth-generation (5g) wireless networks—with a focus on propagation models," *IEEE Transactions on Antennas and Propagation*, vol. 65, no. 12, pp. 6213–6230, 2017.

[45] J. Xu, W. Hong, Z. H. Jiang, and H. Zhang, "Millimeter-wave broadband substrate integrated magneto-electric dipole arrays with corporate low-profile microstrip feeding structures," *IEEE Transactions on Antennas and Propagation*, vol. 68, no. 10, pp. 7056–7067, 2020.

[46] Y. C. Chang, C. C. Hsu, M. I. Magray, H. Y. Chang, and J.-H. Tarng, "A novel dual-polarized wideband and miniaturized low profile magneto-electric dipole antenna array for mmwave 5g applications," *IEEE Open Journal of Antennas and Propagation*, vol. 2, pp. 326–334, 2021.

[47] Z. Lu, Y. Sun, H. Zhu, and F. Huang, "A broadband ±45° dual-polarized magneto-electric dipole antenna for 2g/3g/lte/5g/wimax applications," *Progress In Electromagnetics Research C*, vol. 86, pp. 153–165, 2018.

[48] S. M. Moghaddam, J. Yang, and A. U. Zaman, "Fully-planar ultrawideband tightly-coupled array (fpu-tca) with integrated feed for wide-scanning millimeter-wave applications," *IEEE Transactions on Antennas and Propagation*, vol. 68, no. 9, pp. 6591–6601, 2020.

[49] J. Xu, W. Hong, H. Zhang, G. Wang, Y. Yu, and Z. H. Jiang, "An array antenna for both long- and medium-range 77 ghz automotive radar applications,"

*IEEE Transactions on Antennas and Propagation*, vol. 65, no. 12, pp. 7207–7216, 2017.

[50] M. Ferrando-Rocher, J. I. Herranz-Herruzo, A. Valero-Nogueira, B. Bernardo-Clemente, A. U. Zaman, and J. Yang, "$8 \times 8$ $ka$-band dual-polarized array antenna based on gap waveguide technology," *IEEE Transactions on Antennas and Propagation*, vol. 67, no. 7, pp. 4579–4588, 2019.

[51] L. Shi, C. Bencivenni, R. Maaskant, J. Wettergren, J. Pragt, and M. Ivashina, "High-efficiency and wideband aperiodic array of uniformly excited slotted waveguide antennas designed through compressive sensing," *IEEE Transactions on Antennas and Propagation*, vol. 67, no. 5, pp. 2992–2999, 2019.

[52] S.-G. Zhou, G.-L. Huang, T.-H. Chio, J.-J. Yang, and G. Wei, "Design of a wideband dual-polarization full-corporate waveguide feed antenna array," *IEEE Transactions on Antennas and Propagation*, vol. 63, no. 11, pp. 4775–4782, 2015.

[53] X. Cui, F. Yang, M. Gao, L. Zhou, Z. Liang, and F. Yan, "A wideband magneto-electric dipole antenna with microstrip line aperture-coupled excitation," *IEEE Transactions on Antennas and Propagation*, vol. 65, no. 12, pp. 7350–7354, 2017.

[54] B. Q. Wu and K.-M. Luk, "A broadband dual-polarized magneto-electric dipole antenna with simple feeds," *IEEE Antennas and Wireless Propagation Letters*, vol. 8, pp. 60–63, 2009.

[55] T. Zhang, L. Chen, S. M. Moghaddam, A. Uz Zaman, and J. Yang, "Wideband dual-polarized array antenna on dielectric-based inverted microstrip gap waveguide," in *2019 13th European Conference on Antennas and Propagation (EuCAP)*, 2019, pp. 1–3.

[56] K. Luk and H. Wong, "A new wideband unidirectional antenna element," *Int J Microwave Opt Technol*, vol. 1, 01 2006.

[57] K.-M. Luk and B. Wu, "The magnetoelectric dipole—a wideband antenna for base stations in mobile communications," *Proceedings of the IEEE*, vol. 100, no. 7, pp. 2297–2307, 2012.

[58] M. Li and K.-M. Luk, "Wideband magneto-electric dipole antenna for 60-ghz millimeter-wave communications," *IEEE Transactions on Antennas and Propagation*, vol. 63, no. 7, pp. 3276–3279, 2015.

[59] Y. Shao, X.-C. Li, L.-S. Wu, and J.-F. Mao, "A wideband millimeter-wave substrate integrated coaxial line array for high-speed data transmission," *IEEE Transactions on Microwave Theory and Techniques*, vol. 65, no. 8, pp. 2789–2800, 2017.

[60] J. Liu, A. U. Zaman, and P.-S. Kildal, "Optimizing the numerical port for inverted microstrip gap waveguide in full-wave simulators," in *2016 10th European Conference on Antennas and Propagation (EuCAP)*, 2016, pp. 1–5.

[61] Z. N. Chen, Q. Lou, and W. Liu, "Metantennas: Opportunities and challenges in future microwave metasurface antenna research and applications," in *2022 16th European Conference on Antennas and Propagation (EuCAP)*, 2022, pp. 1–5.

[62] J.-W. Lian, M. Ansari, P. Hu, Y. J. Guo, and D. Ding, "Wideband and high-efficiency parallel-plate luneburg lens employing all-metal metamaterial for multibeam antenna applications," *IEEE Transactions on Antennas and Propagation*, vol. 71, no. 4, pp. 3193–3203, 2023.

[63] F. Ahmed, M. U. Afzal, T. Hayat, K. P. Esselle, and D. N. Thalakotuna, "A near-field meta-steering antenna system with fully metallic metasurfaces," *IEEE Transactions on Antennas and Propagation*, vol. 70, no. 11, pp. 10 062–10 075, 2022.

[64] T. E. J. U. Z. YONG, "Antenna array based on one or more metamaterial structures," U.S. Patent US20220109246A1, June 2022.

[65] D. Chen, W. Yang, W. Che, and Q. Xue, "Broadband stable-gain multiresonance antenna using nonperiodic square-ring metasurface," *IEEE Antennas and Wireless Propagation Letters*, vol. 18, no. 8, pp. 1537–1541, 2019.

[66] F. Mesa, G. Valerio, R. Rodríguez-Berral, and O. Quevedo-Teruel, "Simulation-assisted efficient computation of the dispersion diagram of periodic structures: A comprehensive overview with applications to filters, leaky-wave antennas and metasurfaces," *IEEE Antennas and Propagation Magazine*, vol. 63, no. 5, pp. 33–45, 2021.

[67] Z. H. Jiang, Y. Zhang, J. Xu, Y. Yu, and W. Hong, "Integrated broadband circularly polarized multibeam antennas using berry-phase transmit-arrays for $ka$ -band applications," *IEEE Transactions on Antennas and Propagation*, vol. 68, no. 2, pp. 859–872, 2020.

[68] O. Yesilyurt and G. Turhan-Sayan, "Metasurface lens for ultra-wideband planar antenna," *IEEE Transactions on Antennas and Propagation*, vol. 68, no. 2, pp. 719–726, 2020.

[69] N. Yogesh and Z. Ouyang, *Metamaterial Frequency Selective Surfaces As Polarizers*. Singapore: Springer Nature Singapore, 2020, pp. 1–28. [Online]. Available: https://doi.org/10.1007/978-981-15-8597-5_10-1

[70] Z. Lin, X. Li, and S. He, "High-performance silicon te-pass polarizer assisted by anisotropic metamaterials," *Opt. Express*, vol. 30, no. 14, pp. 24 841–24 851, Jul 2022. [Online]. Available: https://opg.optica.org/oe/abstract.cfm?URI=oe-30-14-24841

[71] M. Alibakhshikenari, M. Khalily, B. S. Virdee, C. H. See, R. A. Abd-Alhameed, and E. Limiti, "Mutual-coupling isolation using embedded metamaterial em bandgap decoupling slab for densely packed array antennas," *IEEE Access*, vol. 7, pp. 51 827–51 840, 2019.

[72] N.-S. Nie, X.-S. Yang, Z. N. Chen, and B.-Z. Wang, "A low-profile wideband hybrid metasurface antenna array for 5g and wifi systems," *IEEE Transactions on Antennas and Propagation*, vol. 68, no. 2, pp. 665–671, 2020.

[73] T. Li and Z. N. Chen, "Shared-surface dual-band antenna for 5g applications," *IEEE Transactions on Antennas and Propagation*, vol. 68, no. 2, pp. 1128–1133, 2020.

[74] J.-W. Lian, D. Ding, and R. Chen, "Wideband millimeter-wave substrate-

integrated waveguide-fed metasurface antenna," *IEEE Transactions on Antennas and Propagation*, vol. 70, no. 7, pp. 5335–5344, 2022.

[75] W. E. I. Liu, Z. N. Chen, and X. Qing, "Broadband low-profile l-probe fed metasurface antenna with tm leaky wave and te surface wave resonances," *IEEE Transactions on Antennas and Propagation*, vol. 68, no. 3, pp. 1348–1355, 2020.

[76] M. Y. Jamal, M. Li, K. L. Yeung, X. Li, L. Jiang, and T. Itoh, "A low-profile fabry–pérot cavity antenna using anisotropic metasurface," *IEEE Antennas and Wireless Propagation Letters*, vol. 21, no. 2, pp. 356–360, 2022.

[77] J. d. Dieu Ntawangaheza, L. Sun, S. Wang, Y. Li, Z. Zheng, D. Biao, and G. Rushingabigwi, "A single-layer low-profile broadband metasurface-inspired antenna with monopole-like radiation characteristics," *IEEE Transactions on Antennas and Propagation*, vol. 70, no. 6, pp. 4818–4823, 2022.

[78] E. R.-I. E. A. P.-S. Kildal, A.U. Zaman and A. Valero-Nogueira, *IET Microwaves, Antennas & Propagation*, vol. 5, pp. 262–270(8), February 2011. [Online]. Available: https://digital-library.theiet.org/content/journals/10.1049/iet-map.2010.0089

[79] P.-S. Kildal, E. Alfonso, A. Valero-Nogueira, and E. Rajo-Iglesias, "Local metamaterial-based waveguides in gaps between parallel metal plates," *IEEE Antennas and Wireless Propagation Letters*, vol. 8, pp. 84–87, 2009.

[80] E. Rajo-Iglesias, M. Ferrando-Rocher, and A. U. Zaman, "Gap waveguide technology for millimeter-wave antenna systems," *IEEE Communications Magazine*, vol. 56, no. 7, pp. 14–20, 2018.

[81] T. Zhang, R. Tang, L. Chen, S. Yang, X. Liu, and J. Yang, "Ultra-wideband full-metal planar array antenna with a combination of ridge gap waveguide and e-plane groove gap waveguide," *IEEE Transactions on Antennas and Propagation*, vol. 70, no. 9, pp. 8051–8058, 2022.

[82] J. Yue, C. Zhou, K. Xiao, L. Ding, and S. Chai, "W-band low-sidelobe series-fed slot array antenna based on groove gap waveguide," *IEEE Antennas and Wireless Propagation Letters*, vol. 22, no. 4, pp. 908–912, 2023.

[83] M. Ferrando-Rocher, A. Valero-Nogueira, J. I. Herranz-Herruzo, A. Berenguer, and B. Bernardo-Clemente, "Groove gap waveguides: A contactless solution for multilayer slotted-waveguide array antenna assembly," in *2016 10th European Conference on Antennas and Propagation (EuCAP)*, 2016, pp. 1–4.

[84] K. F. Renk, *Fabry–Perot Resonator*. Berlin, Heidelberg: Springer Berlin Heidelberg, 2012, pp. 43–54. [Online]. Available: https://doi.org/10.1007/978-3-642-23565-8_3

[85] W. Y. Yong, A. Haddadi, T. Emanuelsson, and A. A. Glazunov, "A bandwidth-enhanced cavity-backed slot array antenna for mmwave fixed-beam applications," *IEEE Antennas and Wireless Propagation Letters*, vol. 19, no. 11, pp. 1924–1928, 2020.

[86] D. Zarifi, A. Farahbakhsh, A. U. Zaman, and P.-S. Kildal, "Design and fabrication of a high-gain 60-ghz corrugated slot antenna array with ridge gap waveguide distribution layer," *IEEE Transactions on Antennas and Propagation*, vol. 64,

no. 7, pp. 2905–2913, 2016.

[87] T. Zhang, R. Tang, L. Chen, S. Yang, X. Liu, and J. Yang, "Ultra-wideband full-metal planar array antenna with a combination of ridge gap waveguide and e-plane groove gap waveguide," *IEEE Transactions on Antennas and Propagation*, vol. 70, no. 9, pp. 8051–8058, 2022.

[88] A. U. Zaman and P.-S. Kildal, "Wide-band slot antenna arrays with single-layer corporate-feed network in ridge gap waveguide technology," *IEEE Transactions on Antennas and Propagation*, vol. 62, no. 6, pp. 2992–3001, 2014.

[89] W. Liu, Z. N. Chen, and X. Qing, "60-ghz thin broadband high-gain ltcc metamaterial-mushroom antenna array," *IEEE Transactions on Antennas and Propagation*, vol. 62, no. 9, pp. 4592–4601, 2014.

[90] W. E. I. Liu, Z. N. Chen, X. Qing, J. Shi, and F. H. Lin, "Miniaturized wide-band metasurface antennas," *IEEE Transactions on Antennas and Propagation*, vol. 65, no. 12, pp. 7345–7349, 2017.

[91] T. Li and Z. N. Chen, "Wideband sidelobe-level reduced $ka$ -band metasurface antenna array fed by substrate-integrated gap waveguide using characteristic mode analysis," *IEEE Transactions on Antennas and Propagation*, vol. 68, no. 3, pp. 1356–1365, 2020.

[92] J. F. Gao and F. H. Lin, "Modeling and analysis of wideband multilayer metasurface antenna array using characteristic-mode analysis," *IEEE Transactions on Antennas and Propagation*, vol. 71, no. 3, pp. 2832–2836, 2023.